Electrodynamics of correlated electron systems:

Lecture Notes 2008 *Boulder summer school on condensed matter physics*

N. P. Armitage[1]
[1]*Department of Physics and Astronomy, The Johns Hopkins University, Baltimore, MD 21218, USA*

(Dated: August 1, 2008)

Contents

Physical and chemical systems can be characterized by their natural frequencies ω and energy scales. It is hardly an exaggeration that most of what we know about such systems, from the acoustics of a violin to the energy levels of atoms, comes from their response to perturbations at these natural frequencies. For instance, chemists and biologists use infrared spectroscopy absorptions around 1650 cm^{-1} (which corresponds to frequencies of 49 THz, wavelengths of 6 μm, and energies of 0.2 eV) to identify the carbon-carbon double bond in organic compounds. And it was the observation of light emission from atoms at discrete energies in the electron Volt range that led to the quantum theory.

It is of course the same situation in 'correlated' electron systems. We learn about the novel effects of strong electron-electron interactions and the properties of collective states of matter by characterizing their response to small amplitude perturbations at their natural frequencies. In solids, these natural frequency scales span an impressively large frequency range from the DC to the x-ray. This incredible range means that a blizzard of experimental techniques and analysis methods are required for the characterization of correlated systems with optical techniques.

These short lecture notes attempt to lay out a brief summary of the formalism, techniques, and analysis used for 'optical' spectroscopies of correlated electron systems. This collection is idiosyncratic, opinionated, and, considering the breadth of the subject, very brief. Unfortunately, there is no single complete treatise yet that presents a complete background for these topics in the context of correlated electron materials. However, there are a number of excellent resources that collectively give a solid background to this field.

I recommend:

1. F. Wooten, "Optical Properties of Solids", (Academic Press, New York, 1972).
   The classic introduction to the subject of the electrodynamic response of solids
2. M. Dressel and G. Grüner, "Electrodynamics of Solids: Optical Properties of Electrons in Matter", (Cambridge University Press, 2002).
   Much newer and modern with many excellent plots of relevant response functions. Treatments of modern subjects such as superconductivity. Already a classic.
3. G. D. Mahan, "Many-Particle Physics", (Plenum, 2nd ed., 1990).
   The go-to resource for pertubative treatments of correlations in solids.
4. Richard D. Mattuck, "A Guide to Feynman Diagrams in the Many-Body Problem", (Dover, 2nd ed., 1992).
   "Feynman diagrams for dummies." Well ... I like it anyways.
5. E. van Heumen and D. van der Marel, "Salerno lectures: Optical probes of electron correlations in solids", Available at `http://optics.unige.ch/vdm/marel_files/salerno_lectures.pdf`
   Excellent lecture notes some of which parallels the treatment here.
6. D. Basov and T. Timusk, "Electrodynamics of high-T_c superconductors", Reviews of Modern Physics **77**, 721 (2005).
   A thorough review of the use of optical probes in the cuprate superconductors.
7. L. Degiorgi, "The electrodynamic response of heavy-electron compounds", Rev. Mod. Phys. **71**, 687 (2005).
8. A. Millis and P.A. Lee, "Large-orbital-expansion

for the lattice Anderson model", Phys. Rev. B **35**, 3394 (1987).
Theoretical paper with an excellent section on the phenomenological expectations for the optical response of heavy fermion materials and optical self-energies.

9. C.C. Homes, "Fourier Transform Infrared Spectroscopy", Lecture notes available here `http://infrared.phy.bnl.gov/pdf/homes/fir.pdf`
A good introduction to various technical issues associated with Fourier Transform Infrared Reflectivity (FTIR); the most commonly used measurement technique for optical spectra of correlated electron systems.
10. George B. Arfken and Hans J. Weber, "Mathematical Methods for Physicists"
The classic textbook of mathematical methods for physicists. Good reference on Kramers-Kronig and Hilbert transforms
11. John David Jackson, "Classical Electrodynamics" (3rd ed., Wiley)
No motivation need be given

Other references as cited below.

I. INTRODUCTION

As mentioned above, the energy and frequency scales relevant for correlated systems span the fantastic range of the DC to the x-ray (Fig. 1). For instance, atomic energy scales of 0.5 eV to the keV, make solids possible through chemical bonding. These energies also manifest themselves explicitly in correlations by, for instance, setting the energy scale of the large on-site repulsions U of electrons which can lead to Mott-Hubbard interactions and insulating states. Typical overlap integrals between atomic wavefunctions in solids are at the low end of the eV energy scale and set the scale of Fermi energies in metals and hence the energy scale for electron delocalization and roughly that also of plasmon collective modes. Various collective modes such as phonons and magnons are found at lower energy scales, typically at fractions of an eV. At energies of order 50 meV are the superconducting gaps of optimally doped cuprates. At even lower energies of the few meV scale the scattering rate of charges in clean metals is found. This is also the energy scales of gaps in conventional superconductors. Many local f-electron orbitals, which are relevant in Kondo materials also have energies found at these energies as well. At even lower energies can be found the width of the 'Drude' peaks found in the AC conductivity of heavy fermion systems. All such energy scales can be studied in many different contexts with various photon spectroscopies.

Although there are many different photon spectroscopies that can be discussed, which span these scales, in these lectures I concentrate on 'optical' spectroscopies, which I define as spectroscopies which involve transitions with net momentum transfer $q = 0$ and whose absorption and polarization properties are governed by the dipole matrix element. I do not discuss the fascinating and important work being done using other photon spectroscopies using light and charge in correlated systems with Raman spectroscopy (1), electron energy loss, Brillouin scattering, optical Kerr rotation, photoemission, and fluorescence spectroscopies to give a very incomplete list. In our case, the quantities of interest are typically the *complex* frequency dependent conductivity $\sigma(\omega)$ or dielectric constant $\epsilon(\omega)$. Alternatively data may be expressed in terms of one of a variety of straightforward complex parametrizations of these quantities like the index of refraction n and absorption coefficient k, or the complex surface impedace Z_s. These quantities are defined for the interaction of light with materials generically from zero frequency to arbitrarily high frequencies. However, in these lecture notes I confine myself to the frequency range from microwaves, through the THz, to infrared, visible and ultraviolet. Each of these regimes gives different kinds of information and requires different techniques. For instance, microwaves are measured in cavities, striplines, or with Corbino techniques. THz is a huge growth area with the advent of time-domain THz and the increased use of Backward Wave Oscillators (BWOs). The infrared and visible range are measured by Fourier Transform Infrared Reflectivity (FTIR). Visible and Ultraviolet can be measured by spectroscopic ellipsometry. Of course there are large overlaps between all these regimes and techniques.

I caution that throughout these lecture notes, I frequently make use of the language of quasi-free electrons with well-defined masses and lifetimes. It is not clear that such a description is automatically valid in correlated systems. In fact, it is not even clear that such a description should be valid in 'normal' materials. Why should an ensemble of 10^{24} electrons/cm^3 interacting with each other *via* long range Coulomb interaction have excitations and states that resemble anything like those of free electrons? Naively one would expect that excitations would be manifestly many-electron composite objects wholly unrelated to the individual particles which constitute the system. It is nothing short of a miracle that, in fact, many materials are relatively well described by the assumption that interactions do not play a principle role in the explicit physics. Low-energy experiments (e.g. DC resistivity, specific heat) on materials like sodium, gold, or silicon indicate that many aspects of such systems can be well described by free-electron physics. The electrons only appear to feel the static field of the ionic cores and the average static effect of the other electrons. In other materials, like for instance the heavy fermion compounds, experiments seem to indicate that the charge carriers are free, but have masses many times larger than that of a bare electron. But even here at the lowest energy scales there are no explicit signs that charger carriers are simultaneously interacting with 10^{23} other charges. In general, it is surprising that considering the close proximity that

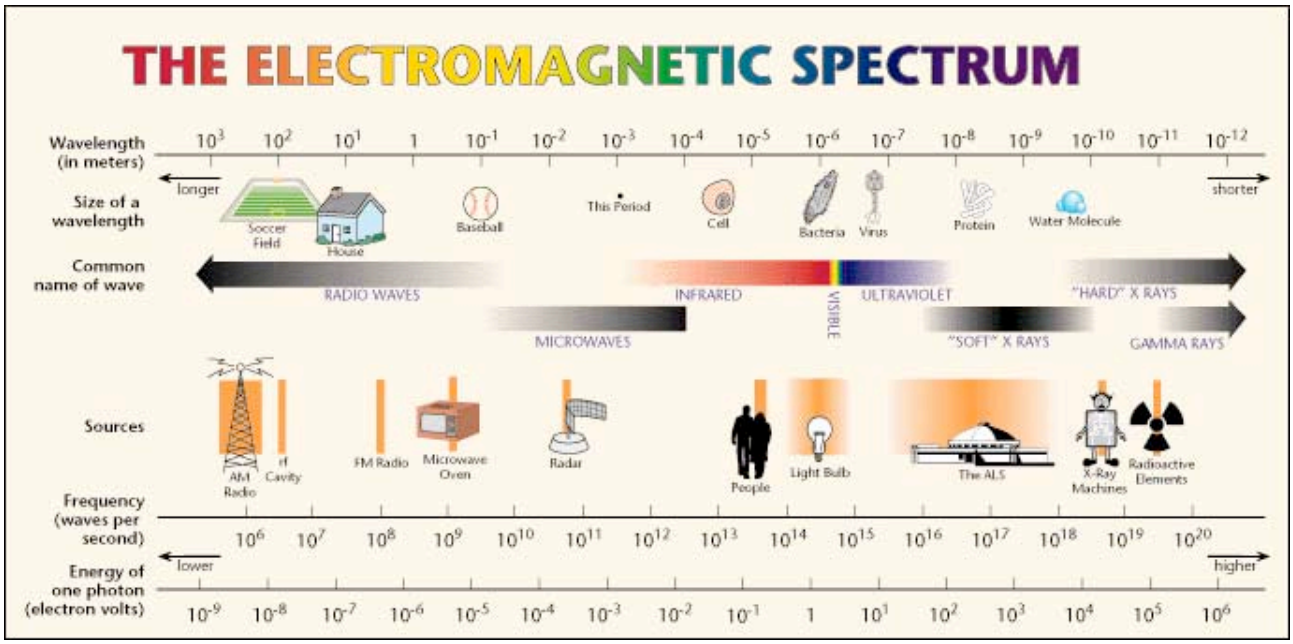

FIG. 1 (Color) The electromagnetic spectrum from radiofrequencies to gamma rays. Diagram from the LBL Advanced Light Source web site `http://www.lbl.gov/MicroWorlds/ALSTool/EMSpec/EMSpec2.html`.

many electrons have to each other that such interactions appear to only be weak perturbations on the free-electron physics.

In a system of interacting fermions, the relatively weak effect that even potentially strong interactions have on the underlying physics can be understood by realizing the strong constraint that a Fermi surface provides on the scattering kinematics. This phase space constriction gives, within the conventional treatment, a scattering rate that goes like $\omega^2 + T^2$ at low frequency and temperature. Due to this quadratic dependence, for some small frequency the particle's scattering rate will be less than its energy and one can say that the quasi-particle excitation is well-defined and scattering is a minor perturbation on the free-electron physics. Such a perturbation renormalizes to zero in the $\omega \to 0$ limit. The effect of interactions can be subsumed into giving quasiparticle excitations a finite lifetime and a renormalized energy parameterized by an effective mass m^*.

Landau hypothesized that if one envisions slowly turning on an interaction potential in a gas of non-interacting electrons, some character of the original system would remain (2). Specifically, he conjectured that there would be a one-to-one correspondence between states and excitations of the non-interacting system and those of the interacting system. In which case there can be said to be an *adiabatic continuity* between the two and one can try to understand and model the interacting system by modeling the non-interacting one. A system with such a mapping is termed a *Fermi-liquid*. And its quasi-free electron-like excitations are termed $quasi-particles$.

The success of Fermi liquid theory comes, as mentioned above, from the constraint on scattering kinematics for low-energy excitations. This gives the result that quasi-particle excitations are only defined at arbitrarily small energy scales. The condition for well defined quasiparticles to exists, $\beta\omega^2 \ll \omega$, means that as one increases the parameter β, which characterizes the strength of electron-electron excitations, the maximum energy of well-defined excitations decreases, but well-defined quasiparticles will still exist at low energies. Within this view, stronger interactions mean only that Fermi liquid behavior will occur at lower-energy scales i.e. at lower temperatures and excitation energies.

Systems for which the Fermi-liquid paradigm is valid can be described at low energies and temperatures in terms of quasi-free electrons. Although the vast majority of normal metallic systems do seem to obey the Fermi liquid phenomenology, it is unclear whether such a description is valid for correlated electron systems. A violation could occur for instance in Hubbard models when the intersite hopping parameter t, which parameterizes the band width, is much smaller than the onsite Coulomb interaction U resulting in an insulating state. So far the fractional quantum Hall effect is the only case where Landau's conjecture regarding a one-to-one correspondence of states has been *experimentally* falsified (3; 4). On the theoretical side, exact solutions to 1D interacting models also show definitively that the fundamental excitations in 1D are not electron-like at all, but are fractions of electrons: spinons and holons that carry spin and charge separately (5). This would be another case where the electronic quasiparticle concept is not valid, but thus far in real systems the residual higher dimensionality has

been found to stabilize the Fermi liquid (See for instance Ref. (6)).

It is true that many systems that we call strongly correlated exhibit a phenomenology inconsistent with the Fermi-liquid paradigm. It is unclear whether this is because interactions have driven such materials truly into a non-Fermi liquid state or because other effects cover up what would be otherwise Fermi liquid phenomena at the experimentally accessible temperatures and frequencies is unclear. For instance, it is important to keep in mind that the much heralded non-Fermi liquid behavior of high T_c cuprates is actually exhibited at relatively high temperatures ($\sim$100 K) above the occurence of superconductivity. It may be that the inopportune occurrence of superconductivity obstructs the view of what would be the low-energy quasiparticle behavior.

At this point it is unclear to what extent the Fermi liquid paradigm applies to many of the materials being given as examples below. In this regard, one must keep in mind, that much of the language tossed around in this field presupposes the validity of it and the existence of well-defined electronic excitations. Indeed, much of the terminology used in the field shows this bias. The terms 'density of states', 'effective mass', 'scattering rate', 'Pauli susceptibility', 'band structure', 'electron-phonon' coupling all require the context of the Fermi liquid to make sense. Clearly such language is inappropriate if such excitations and states do not exist! In the literature one sees many papers discussing, for instance, optical or photoemission electronic self-energies, while at the same time the authors discuss the non-Fermi liquid aspect of these materials. It is not clear whether it is appropriate to discuss electronic self-energies in materials where the elementary excitations are not electron-like. It is the case that while the formalism for generating electronic self-energies from optical or photoemission data as discussed below may be followed straightforwardly, the physical signficance of such self-energies is not clear. For instance, although the parametrizations of optical spectra in terms of the frequency dependent mass and scattering rate from the extended Drude model (see below) can always be valid as a *parameterization*, it is probable that one can only assign physical significance to these quantities if the quasi-particle concept is valid in the energy range of interest.

Some aspects of the below formalism is model independent and some rests on the concept of well-defined electronic Fermi-liquid excitations. Although I will try to make the various distinctions clear, I use the language of quasi-free electrons almost entirely throughout the below, because at the very least it provides a rough intuition of the kinds of effects one expects in insulator, metals, and superconductors. It also provides a self-contained formalism for the analysis of optical spectra. A generalization of these ideas to strongly correlated systems does not currently exist. In the spirit of learning to walk before one learns to run, we use the ideas and language of quasi-free electrons in these lecture notes throughout, but I caution on the naive application of these ideas, which are only formally true for non-interactings systems to strongly interacting ones! The generalization to non-Fermi liquid, correlated, strongly interacting etc. etc. systems is left as an excercise for the reader!!!

II. FORMALISM

A. Optical Constants of Solids

Any discussion of the interaction of light with matter starts with Maxwell's equations

$$\nabla \cdot E(r,t) = 4\pi\rho(r,t), \tag{1}$$

$$\nabla \times E(r,t) = -\frac{1}{c}\frac{\partial}{\partial t}B(r,t), \tag{2}$$

$$\nabla \cdot B(r,t) = 0, \tag{3}$$

$$\nabla \times B(r,t) = \frac{1}{c}\frac{\partial}{\partial t}E(r,t) + \frac{4\pi}{c}J(r,t). \tag{4}$$

where E and B represent the electric and magnetic fields averaged over some suitable microscopic length, typically the incident light wavelength. As usual we introduce auxiliary fields as

$$D = E + 4\pi P, \tag{5}$$

$$H = B - 4\pi M. \tag{6}$$

where D and H have their usual definitions and M and P are magnetization and polarization. Using the continuity equation for the electric current $\nabla \cdot J = -\frac{\partial \rho}{\partial t}$ and accounting for all sources for free conduction, polarization, and magnetization currents $J_{tot} = J_{cond} + \frac{\partial P}{\partial t} + c\nabla \times M$ as well as the external and induced charges $\rho_{total} = \rho_{ext} + \rho_{ind}$ we get the additional equations (please refer to Jackson for a more extended discussion).

$$\nabla \cdot D = 4\pi\rho_{ext}, \tag{7}$$

$$\nabla \times H = \frac{1}{c}\frac{\partial D}{\partial t} + \frac{4\pi}{c}J_{ext} + \frac{4\pi}{c}J_{cond}. \tag{8}$$

Here we assume that we are in the linear regime and the response of polarization, or magnetization of current is linear in the applied field. We therefore write

$$\begin{aligned} P &= \chi_e E, \\ M &= \chi_m H, \\ J &= \sigma E. \end{aligned} \tag{9}$$

Typically we express the electric and magnetic susceptibilities in terms of dielectric functions $\epsilon = 1 + 4\pi\chi_e$ and magnetic permittivity $\mu = 1 + 4\pi\chi_m$. Except for explicitly magnetic materials, $\chi_m = 0$. The dielectric function is a response function that connects the field E at some

time t and position r with the field D at some later time and position. Generally we first define it in the time and position domain *via* the relation

$$D(r,t) = \int_{-\infty}^{t} \int \epsilon(r,r',t,t')E(r',t')d^3r'dt'. \quad (10)$$

One could also describe the system's response in terms of current and conductivity $\sigma(\omega)$

$$J(r,t) = \int_{-\infty}^{t} \int \sigma(r,r',t,t')E(r',t')d^3r'dt'. \quad (11)$$

In this context, the real space and time dependent ϵ and σ are usually referred to as *memory* functions for obvious reasons. For analysis of optical spectra we are typically more interested in their Fourier transforms. The quantities $\sigma(q,\omega)$ and $\epsilon(q,\omega)$ are related by

$$\sigma = \frac{i\omega}{4\pi}(1-\epsilon). \quad (12)$$

One frequently sees the complex response functions written using the real part of the conductivity and the real part of the dielectric function e.g. $\epsilon = \epsilon_1 + i4\pi\sigma_1/\omega$.

Given the very general form of Eqs. 10 and 11, simple physical considerations allow a number of general statements to be made. First, due to the vast mismatch between the velocity of light and the typical velocity of electrons in solids, we are typically concerned with the $q = 0$ limit of their Fourier transforms. This means that except in a few circumstances, where one must take into account non-local electrodynamics, (very clean metals or superconductors for instance), one can assume that down to the scale of some microscopic length there is a local relationship between the quantities given in Eqs. 9. This means that while these quantities may have spatial dependence (for instance the current J is confined to surfaces in metals), the proportionality expressed in Eq. 9 holds. One can use the above expressions to rewrite Maxwell's equations explicitly in terms of ϵ, μ and σ. (Please see Jackson for further details.)

Furthermore, the principle of causality - that effects can not proceed their causes - demands strict temporal considerations regarding the integrals in Eqs. 10 and 11. This leads to the powerful Kramers-Kronig relations relating the real and imaginary part of such response functions. We can rewrite Eq. 11 as

$$J(t) = \int_{-\infty}^{t} \sigma(t-t')E(t')dt'. \quad (13)$$

From causality the conductivity memory function $\sigma(t-t')$ has the property that $\sigma(\tau < 0) = 0$. The Fourier transform of $\sigma(t-t')$ is then

$$\sigma(\omega) = \int_{0}^{t} \sigma(\tau)e^{i\omega\tau}d\tau. \quad (14)$$

The integral can be performed in the complex frequency plane with the substitution $\omega \to z = \omega_1 + i\omega_2$. It is then written

$$\sigma(\omega) = \int_{0}^{\infty} \sigma(\tau)e^{i\omega_1\tau}e^{-\omega_2\tau}d\tau. \quad (15)$$

The second exponent in this integral is bounded in the upper half of the complex plane for $\tau > 0$ and in the lower half plane for $\tau < 0$. Since $\sigma(\tau < 0) = 0$, this means that $\sigma(\omega)$ is analytic for the upper half of the complex plane. This means that Cauchy's theorem applies and therefore

$$\oint \frac{\sigma(\omega')}{\omega' - \omega_0}d\omega' = 0 \quad (16)$$

holds in the upper half of the complex plane in the usual way (Please see Jackson or Arfken for further details on the integration and derivation of the Kramers-Kronig relations). This gives the expression

$$P\int_{-\infty}^{\infty} d\omega' \frac{\sigma(\omega')}{\omega' - \omega} - i\pi\sigma(\omega) = 0, \quad (17)$$

where P as usual denotes the principal part.

From this the Kramers-Kronig relations can be inferred. Using the fact that in the time domain Im $\sigma(\tau) = 0$ then $\sigma(-\omega) = \sigma^*(\omega)$ we can write a simpler form of them as

$$\sigma_1 = \frac{2}{\pi}P\int_{0}^{\infty} d\omega' \frac{\omega'\sigma_2(\omega')}{\omega'^2 - \omega^2}, \quad (18)$$

$$\sigma_2 = -\frac{2\omega}{\pi}P\int_{0}^{\infty} d\omega' \frac{\sigma_1(\omega')}{\omega'^2 - \omega^2}. \quad (19)$$

The Kramers-Kronig relations are tremendously useful in the analysis and determination of optical spectra. When one knows one component of a response function for all frequencies, the other component automatically follows. As will be discussed below, they are used extensively in Fourier Transform Infrared Reflectivity (FTIR) measurements to determine the complex reflectivity (amplitude and phase), by only measuring reflected power.

The above discussion was based on some generalized frequency dependent conductivity $\sigma(\omega)$ and its model independent properties. In real materials, one has a zoo of different possible contributions to the electromagnetic response. In simple metals with periodic translational symmetry (i.e. a crystal), one can identify a number of absorptions that satisfy the $q = 0$ constraint. For instance, for the schematic band structure shown in Fig. 2, one expects a broad feature at finite energy (in red)

in the optical conductivity, which comes from the sum over all possible direct interband band absorptions (red arrow) in which electrons are promoted from below E_F across an energy gap to a higher lying band, with zero net momentum change. Near E_F absorptions with low but finite ω (green arrow) are only possible if strict translational symmetry has been broken by, for instance, disorder. Electrons moving in Bloch waves with mean free path ℓ, can violate strict momentum conservation in optical absorption at momentum scales on the order of $2\pi/\ell$. One can think of this heuristically as smearing out the band structure on this scale. This gives a peak centered at zero frequency (in green). In limit of perfect translational symmetry this peak would be a delta function centered at $\omega = 0$. One can also have excitations of harmonic waves of the lattice (phonons) if such phonons posses a net dipole moment in the unit cell. They appear as distinct and frequently very sharp peaks in the optical conductivity (in blue).

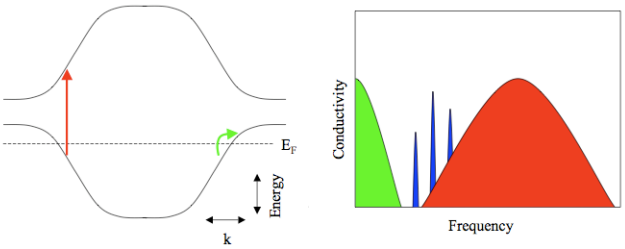

FIG. 2 (Color) Various different optical absorptions that satisfy the $q = 0$ constraint of optical spectroscopy can appear in the optical conductivity of simple metals. Near E_F intraband absorptions (green). Interband absorptions (red). Phonons (blue)

Having introduced the general idea of optical response functions, I now discuss the derivation of them, both classically and quantum mechanically.

B. Classical Treatments: Drude-Lorentz

Almost the simplest model of charge conduction we can conceive of is of a single charge e, driven by an electric field E, and subject to a viscous damping force that relaxes momentum on a time scale τ. Consider the force equation describing this situation

$$mx'' = -eE - mx'/\tau. \tag{20}$$

If we assume harmonic motion then $x = x_0 e^{-i\omega t}$ and $E = E_0 e^{-i\omega t}$. Substituting in for x and E and solving for x_0' we get

$$x_0' = \frac{e\tau E_0}{m}\frac{1}{1 - i\omega\tau}. \tag{21}$$

If we then consider an ensemble of such charges with density N, and realize that the maximum current density is $J_0 = Nex_0'$, we get the relation

$$J_0 = \frac{Ne^2\tau E_0}{m}\frac{1}{1 - i\omega\tau}. \tag{22}$$

Using the previously defined relation $J = \sigma E$ we find the relation for the frequency dependent Drude conductivity is

$$\sigma(\omega) = \frac{Ne^2\tau}{m}\frac{1}{1 - i\omega\tau} = \frac{Ne^2\tau}{m}\frac{1 + i\omega\tau}{1 + \omega^2\tau^2}. \tag{23}$$

Interestingly, this classical model, first conceived of by Paul Drude, is actually of great use even in the analysis of particles obeying quantum mechanical statistics. As discussed below one finds the same functional form to leading order in that case as well.

The Drude model demonstrates a number of important features that are found generally in response functions. Its limit at $\omega \to 0$ is $Ne^2\tau/m$ is well behaved mathematically and equivalent to the DC value. As shown in Fig. 3, it has real and imaginary components that differ from each other. At low frequency the current's response is in phase with the driving field and purely dissipative (real). At intermediate frequencies (when the driving frequency equals the scattering rate $1/\tau$), the real conductivity falls to half its DC value and imaginary conductivity peaks and is equal to the real value. At higher frequencies, two things happen. Not only does the current begin to lag the driving field, but also the overall magnitude of the response has a harder time keeping up with the driving electric field. The conductivity also exhibits distinct power laws in its various frequency limits: linear for the imaginary part at low ω, $1/\omega$ at high ω, and $1/\omega^2$ for the real part at high frequency.

In the limit of zero dissipation $1/\tau \to 0$ we have

$$\sigma_1 = \frac{\pi}{2}\frac{Ne^2}{m}\delta(\omega = 0), \tag{24}$$

$$\sigma_2 = \frac{Ne^2}{m\omega}. \tag{25}$$

σ_1 is zero everywhere, but at $\omega = 0$. As σ_1 is proportional to dissipation, this demonstrates that a gas of collisionless electrons cannot absorb photons at finite frequency. This can be shown directly by demonstrating that the Hamiltonian that describes this interaction, commutes with the momentum operator p and hence it has no time dependence. Electron-electron interactions without umklapp scattering do not change this situation, as such interactions cannot degrade the total system momentum.

The dependence of the Drude conductivity on τ, N, and m, shows that the optical mass of charge carriers in metals can be obtained if for instance the charge density is known by other techniques like the Hall coefficient.

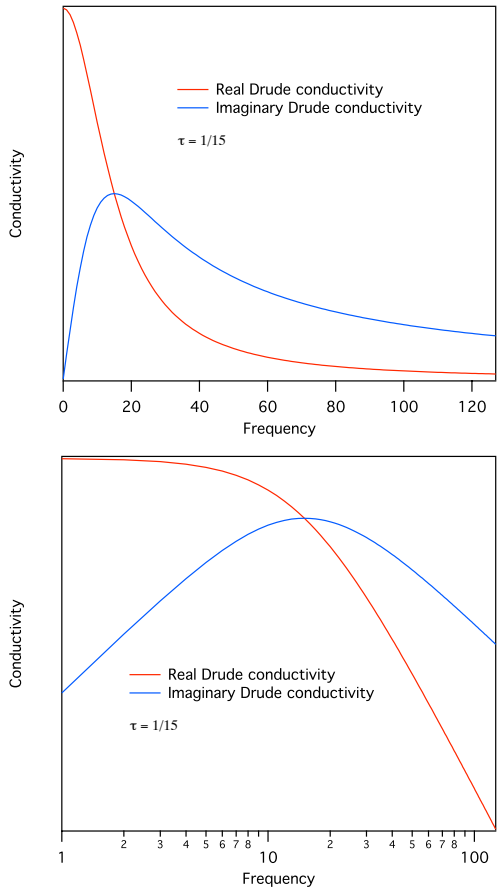

FIG. 3 (Color) Frequency dependent Drude conductivity with scattering rate $1/\tau = 15$ on linear scale (top) log-log scale (bottom).

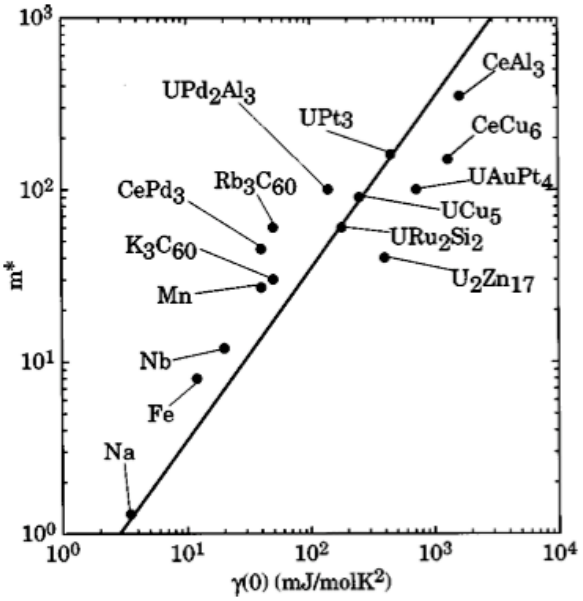

FIG. 4 (Color) Specific-heat values γ vs effective mass m^*, evaluated from the optical data using spectral-weight arguments (7)

For instance, in Fig. 4 the mass determined by optical conductivity is plotted against the linear coefficient in the specific heat (which is proportional to the electronic density of states and hence the mass). From simple metals to exotic heavy fermion materials, it shows a dramatic linear dependence over 3 orders of magnitude.

It is convenient to express the prefactors of the Drude conductivity in terms of the so-called *plasma frequency* $\omega_p = \sqrt{\frac{4\pi N e^2}{m}}$. The plasma frequency is equivalent to the frequency of the free longitudinal oscillations of the electron gas. It reads

$$\sigma(\omega) = \frac{\omega_p^2}{4\pi} \frac{\tau}{1 - i\omega\tau}. \tag{26}$$

Therefore within the Drude model, the optical response is fully determined by two frequencies: the plasma frequency ω_p and the scattering rate $1/\tau$. Since ω_p is many orders of magnitude greater than $1/\tau$, this allows us to define three distinctly different regimes for the optical response.

At low frequencies $\omega \ll 1/\tau$, in the so-called *Hagen – Rubens* regime, the conductivity is almost purely real, frequency independent, and approximately equal to the DC value. At higher frequencies, in the *relaxation regime* where ω is on the order of $1/\tau$, one must explicitly take into account the $\omega\tau$ factor in the denominator of Eq. 23. As mentioned above, in this range the real conductivity falls to half its DC value and imaginary conductivity peaks and is equal to the real value. The significance of the high frequency regime $\omega > \omega_p$ can be seen in rewriting the conductivity as the dielectric function. It is

$$\epsilon(\omega) = 1 - \frac{\omega_p^2}{\omega^2 - i\omega/\tau}. \tag{27}$$

The real and imaginary parts of this expression are given in Fig. **??**. One sees that for the conventional case where $\omega_p \gg 1/\tau$, the plasma frequency is the frequency at which the real part of the dielectric function changes sign from negative to positive. ω_p sets the scale for the zero crossing of ϵ_1. An analysis of the reflection and transmission using the *Fresnel* equations (see Jackson), shows that above the zero crossing, metals described by the Drude model become transparent. Hence this high frequency regime is called the *transparent* regime.

Despite its classical nature, the Drude model describes the gross features of many metals at low frequencies quite well. We give a number of examples of its use and extensions below. Of course, our interest in the electrodynamics of solids extends far beyond the case of simple metals. And even for 'simple' metals, one has the interesting aspects of finite frequency absorptions that parameterize

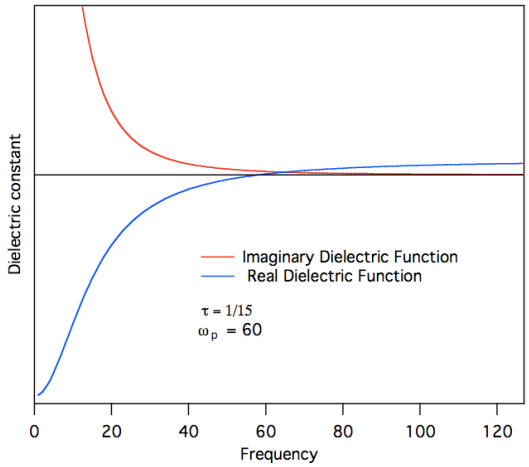

FIG. 5 (Color) Frequency dependent Drude dielectric function with scattering rate $1/\tau = 15$ and plasma frequency $\omega_p = 60$. The real part of the dielectric function changes sign at ω_p.

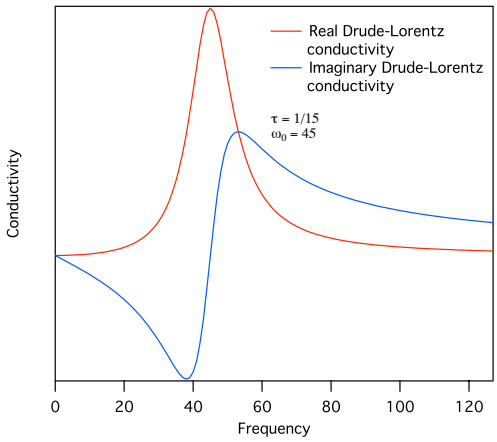

FIG. 6 (Color) Frequency dependent Drude-Lorentz complex conductivity with scattering rate $1/\tau = 15$ and oscillator resonant frequency $\omega_0 = 45$. The real conductivity is zero at $\omega = 0$ and positive for all frequencies.

band structure and, for instance, give copper and gold their beautiful colors. The Drude model is wholly inadequate to describe such finite frequency absorptions. For such processes in more complicated metals, semiconductors, and insulators, one can model them quantum mechanically in a number of ways, but we can also gain predictive power and intuition from an extension to the classical Drude model called *Drude-Lorentz*.

Here we envision the electrons are also subject to a simple harmonic restoring force $-Kx$. Of course, such a model is *physically* inadequate to describe finite frequency absorption in semiconductors and insulators, as their insulating nature is due to the properties of filled bands and not the localization of electrons. Nevertheless, numerous aspects of absorption at 'band-edges' in semiconductors can be modeled phenomenologically with Drude-Lorentz. Of course its applicability to model harmonic phonon absorptions is obvious.

With $\omega_0^2 = K/m$, we extend Eq. 20 as

$$mx'' = -eE - mx'/\tau - \omega_0^2 x, \tag{28}$$

Proceeding in exactly the same fashion as for the simple Drude model, we obtain for the conductivity

$$\sigma(\omega) = \frac{Ne^2}{m}\frac{\omega}{i(\omega_0^2 - \omega^2) + \omega/\tau}, \tag{29}$$

One can see that in the limit $\omega_0 \to 0$ the Drude relation is obtained.

As mentioned above, despite its classical nature and the inapplicability of the underlying physical picture, in some cases the Drude-Lorentz model can be used to quantify finite frequency absorptions. In the case of the band edge absorption in semiconductors, a number of oscillators of the form of Eq. 29 with different weights can be used to capture the decidely non-Lorentzian line shape. One can convince oneself that since any lineshape can be fit arbitrarily well using a arbitrarily large number of oscillators and moreover since the imaginary part of the response follows from a Kramers-Kroning transform of the real part, it is always perfectly feasible to parametrize the response using Drude-Lorentz.

C. The Quantum Case

The above Drude and Drude-Lorentz models are classical models used to describe intrinsically quantum mechanical phenomena and the fact that they are useful at all is surprising. It is clear that a quantum mechanical treatment is desired. The most commonly used method for the quantum mechanical calculation of electromagnetic response of materials is the *Kubo* formalism. It is based on the fluctuation-dissipation theorem, which relates the spontaneous fluctuations of a system described through its correlation functions to its driven linear response.

The interaction Hamiltonian for charge with the electromagnetic field to first-order in field is

$$H_i = \frac{e}{2mc}\sum_{i=1}^{N}[p_i \cdot A(r_i) + A(r_i) \cdot p_i] - e\sum_{i=1}^{N}\Phi(r_i), \tag{30}$$

where p, A, and Φ are the quantum mechanical operators for momentum, vector potential, and scalar potential. Since the vector potential A depends on position, it does not in general commute with p. However since $p = -i\hbar\nabla$, one can show that $p \cdot A - A \cdot p = -i\hbar\nabla \cdot A$ and within the Coulomb gauge $\nabla \cdot A = 0$, p and A do in fact

commute. This means that for purely transverse waves with $\Phi = 0$ the interaction Hamiltonian simplifies to

$$H_i^T = \frac{e}{mc}\sum_{i=1}^{N} p_i \cdot A(r_i). \quad (31)$$

By substituting in for the canonical momentum $p = mv - eA/c$, dropping all terms that are higher than linear in A, and replacing the summations by an integral one can show that H_i takes the form

$$H_i^T = -\frac{1}{c}\int dr J^T(r) \cdot A^T(r). \quad (32)$$

This gives a Fourier transformed quantity of

$$H_i^T = -\frac{1}{c} J^T(q) \cdot A^T(q). \quad (33)$$

Next we calculate the absorption rate of a system based on the power dissipated $P = \sigma_1 E^2$. We use Fermi's Golden rule to calculate the scattering probablility that incident radiation excites an electron from one state $|s\rangle$ to another $|s'\rangle$.

$$W_{s\to s'} = \frac{2\pi}{\hbar^2}|\langle s'|H_i^T|s\rangle|^2 \delta(\omega - \omega_{s'} + \omega_s). \quad (34)$$

Note that the orbitals $|s\rangle$ and $|s'\rangle$ do not necessarily have to be single-particle states of the system. They are the system's eignestates, which can include the effects of many body physics. Also note that this formula is valid not only at zero temperature, but also at finite temperatures if the bracket is interpreted as a thermodynamic average.

The matrix element follows from the form of H_i^T. It is

$$\langle s'|H_i^T|s\rangle = -\frac{1}{c}\langle s'|J^T(q)|s'\rangle A^T(q). \quad (35)$$

which leads to

$$W_{s\to s'} = \frac{2\pi}{\hbar^2 c^2}\langle s'|J^T(q)|s\rangle\langle s|J^{T*}(q)|s\rangle, \quad (36)$$
$$|A^T(q)|^2 \delta(\omega - \omega_{s'} + \omega_s).$$

where $J^{T*}(q) = J^T(-q)$. One then sums over all occupied initial and all empty final states $W = \sum_{s,s'} W_{s\to s'}$. The dissipated power per unit time and volume at a particular photon frequency ω follows after a few essentially mathematical steps as (see Dressel and Grüner (8))

$$P = \hbar\omega W = \quad (37)$$
$$|A^T(q)|^2 \sum_s \frac{\omega}{\hbar c^2}\int dt\langle s|J^T(q,0)J^{T*}(q,t)|s\rangle e^{-i\omega t}$$

For transverse EM waves, the electric field is related to the vector potential as $E^T = i\omega A^T/c$. Upon substitution we get the absorbed power per unit volume per unit time expressed as a current-current correlation function

$$P = |E^T(q)|^2 \sum_s \frac{1}{\hbar\omega}\int dt\langle s|J^T(q,0)J^{T*}(q,t)|s\rangle e^{-i\omega t}. \quad (38)$$

Using our previously given relation $P = \sigma_1 E^2$, the expression for the real part of the conductivity follows

$$\sigma_1^T(q,\omega) = \sum_s \frac{1}{\hbar\omega}\int dt\langle s|J^T(q,0)J^{T*}(q,t)|s\rangle e^{-i\omega t}. \quad (39)$$

The imaginary part of $\sigma(\omega)$ follows from the Kramers-Kronig relation. This is the *Kubo* formula. It has the form expected for the fluctuation-dissipation theorem, that of a correlation function averaged over all the states of the system $|s\rangle$ and describes fluctuations of the current in the ground state. The conductivity depends on the time correlation between current operators integrated over all times.

The above formalism is general and applies to any set of system states $|s\rangle$. An extension can be made in cases where Fermi statistics applies. The end result is (see Dressel and Grüner (8) for the full derivation)

$$\sigma_1^T(\omega) = \frac{\pi e^2}{m^2\omega}\frac{2}{(2\pi)^3}|\langle s'|p|s\rangle|^2 D_{s's}(\hbar\omega). \quad (40)$$

Here $\langle s'|p|s\rangle$ is known as the dipole matrix element. $D_{s's}$ is the so-called joint density of states, defined as $\frac{2}{(2\pi)^3}\int \delta(\hbar\omega - \hbar\omega_{s's})dk$.

This equation, which is often referred to as the *Kubo-Greenwood* formula is extremely useful for the calculation of higher lying interband transitions in metals and semiconductors when the states $|s\rangle$ and $|s'\rangle$ belong to different bands (as for instance illustrated by the red arrow in Fig. 2). It has the form that one may naively expect; it is proportional to the joint density of states and a matrix element which incorporates aspects like allowed transitions due to symmetry.

We can use the Kubo formalism Eq. 39 to calculate the leading order metallic conductivity in a more rigorous fashion than was done in the classical approach above. We start with Eq. 39 and then posit as an ansatz that finite currents relax as

$$J(q,t) = J(q,0)e^{-t/\tau}. \quad (41)$$

and assume that the current correlation time τ has no dependence on q. Inserting this into the Kubo formula, one gets that

$$\sigma_1(q,\omega) = \frac{1}{\hbar\omega}\sum_{s'}\int dt e^{-i\omega t - |t|/\tau}\langle s|J^2(q)|s'\rangle. \quad (42)$$

One now needs an expression for the current fluctuations at finite q. Of course, the average J is zero, but fluctuations lead to an expectation for a finite $\langle J^2 \rangle$. For small q, one can show in the dipole approximation that $J(q) = -\frac{e}{m}\sum_j p_j$ where j labels the individual particles. With the insertion of a complete set of states s' one gets the expression

$$\sigma_1(q,\omega) = \frac{e^2}{m^2\hbar\omega}\int dt e^{-i\omega t - |t|/\tau}\sum_{s,s',j}|\langle s'|p_j|s\rangle|^2. \quad (43)$$

The quantity $2\sum_{s,s',j}|\frac{|\langle s'|p_j|s\rangle|^2}{m\hbar\omega_{s,s'}}$ found in Eq. 43 is called the *oscillator strength* $f_{s,s'}$. Here ω in Eq. 43 is the energy difference between states $|s\rangle$ and $|s'\rangle$ as is $\omega_{s,s'}$ in the definition of the oscillator strength. Below, we pay special attention to the oscillator strength when we calculate the conductivity sum rules.

The oscillator strength can be easily calculated for the case of free electrons where the energy is $\hbar\omega = \frac{\hbar k^2}{2m}$ and the average momentum is $|\langle s'|p_j|s\rangle|^2 = \frac{\hbar^2 k^2}{4}$. In such a case $f_{s,s'} = N$ the total number of free charge carriers. The final result for the leading order conductivity calculated *via* the Kubo formalism is

$$\sigma_1^{Kubo}(\omega) = \frac{Ne^2\tau}{m}\frac{1}{1-i\omega\tau}, \quad (44)$$

which is the exact same result as calculated classically *via* the Drude model above. For more details see the chapters in Mahan (10).

III. TECHNIQUES

As mentioned above, the incredibly large spectral range spanned by the typical energy scales of solids means that many different techniques must be used. Below I discuss the most used techniques of microwave measurements, THz spectroscopies, optical reflectivity, and ellipsometry that are used to span almost six orders of magnitude in measurement frequency. These various regimes are loosely defined below, but of course there are overlaps between them.

Although I don't discuss them, one might naturally include various radio frequency techniques in this list (which would increase the frequency range by another three orders of magnitude at least). At typical experimental temperatures, the low frequency available in techniques like mutual inductance measurements allows almost the DC limit of quantities like the superfluid density in superconductors to be measured. Interested readers are directed to Ref. (9) and reference therein.

A. Microwaves

Until recently measurements in the microwave range (100 MHz - 100 GHz) were almost entirely done using microwave cavity resonator techniques. Of course, at lower frequencies (kHz and MHz), measurements can be performed by attaching contacts to samples and the complex conductivity can be measured by lock-in techniques, network analyzers, and impedance analyzers. Such methods become problematic in the GHz range however, because wavelengths become comparable to various measurement dimensions (sample size, microwave connector dimensions, cable lengths), and capacitive and inductive effects become appreciable.

In microwave cavity resonance techniques, one is less sensitive to such considerations as the sample forms part of a resonance circuit, which dominates the measurement configuration. Typically one measures transmission through a cavity, which is only possible when at resonance. The technique is widely used for the study of dielectric and magnetic properties of materials in the GHz range, because of its high sensitivity and relative simplicity.

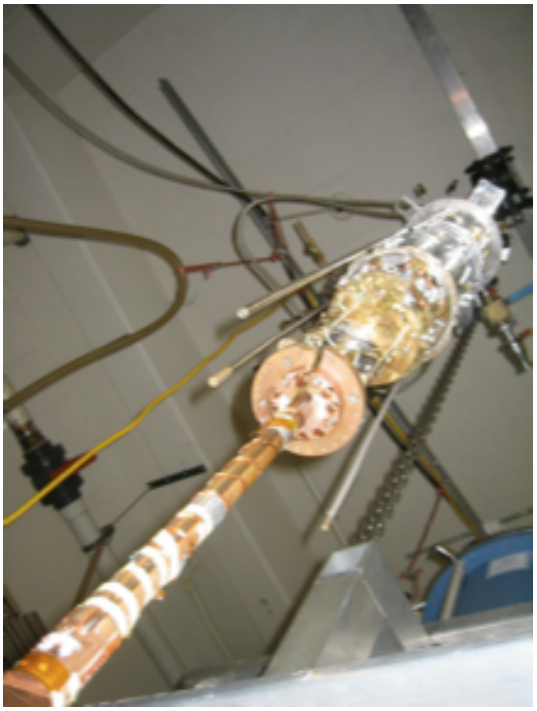

FIG. 7 (Color) View of the UCLA He3 CryoMag system. Cavities can be interchanged quickly to enable a number of different frequencies to be accessed.

A microwave resonator is an enclosed hollow space of cylindrical or rectangular shape machined from high-conductivity metal (typically copper or superconducting metals) with interior dimensions comparable to the free-space wavelength. On resonance, an electromagnetic standing wave pattern is set up inside the cavity. One characterizes the resonance characteristics of the cavity, both with and without a sample inside. Upon sample introduction the center frequency of the resonance shifts and it broadens. From the shifting and broadening, one

can define a complex frequency shift, which with knowledge of the sample size and shape allows one to quantify the complex conductivity directly. For instance, in the limit of very thin films, the center frequency shift is proportional to σ_2 and the broadening is proportional to σ_1. For samples much thicker than the skin or penetration depth, different relations apply (11). The technique does have the considerable disadvantage that only discrete frequencies are measurable, as one is limited to the standing wave resonance frequencies of the cavity, which means that true spectroscopy is not possible. In such measurements one typically determines a sample's complex conductivity as a function of temperature at some finite fixed frequency.

In contrast, the Corbino geometry is a measurement configuration, which is capable of *broadband* microwave spectroscopy. It is compatible with low T and high field cryogenic environments and capable of broadband microwave spectroscopy measurements from 10 MHz to 40 GHz. It is relatively a new technique, but one which has recently been used with great success by a number of groups in the correlated electron physics community (12–17). Although powerful, it has the disadvantage that its use is confined to samples which have typical 2D resistance within a few orders of magnitude of 50 Ohms.

In a Corbino geometry spectrometer a microwave signal from a network analyzer is fed into a coaxial transmission line. A schematic is shown in Fig. 8 (left). The signal propagates down the coaxial line and is reflected from a sample that terminates an open ended coaxial connector. The network analyzer determines the complex reflection coefficient S_{11} of the sample which can be related to the complex sample impedance Z_L *via* the relation $S_{11} = \frac{Z_L - Z_0}{Z_L + Z_0}$ where Z_0 is the coaxial line impedance (nominally 50 Ω). Because the sample geometry is well defined, knowledge of the sample impedance yields intrinsic quantities like the complex conductivity. In the typical case of a thin film where the skin or penetration depth is much larger than the sample thickness d, the sample impedance is related in a straightforward fashion to the complex conductivity as $\sigma = \frac{\ln(r_2/r_1)}{2\pi d Z_L}$ where r_1 and r_2 are the inner and outer conductor radii respectively.

An experimental challenge in Corbino geometry measurements is that the coaxial cables and other parts of the transmission lines can have strongly temperature dependent transmission characteristics. Errors in the intrinsic reflection coefficient, coming from standing wave reflections or phase shifts and damping in the transmission lines, are accounted for by performing a number of calibration measurements. It is imperative that the same cryogenics conditions are reproduced between calibration and each subsequent measurement. In general this is easily done by ensuring the same starting conditions and using a computer controlled cool-down cycle. Recently it has been demonstrated that a three sample calibration (open, short, and a standard 50 ohm resistor) at all temperatures dramatically increases the precision of the technique over previous single sample calibrations(12).

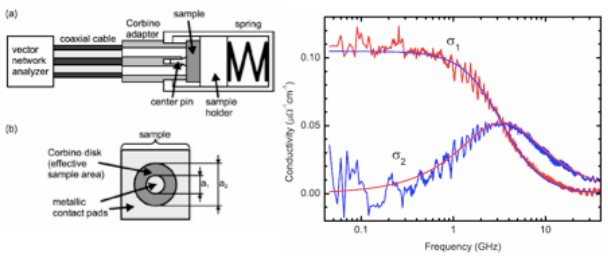

FIG. 8 (Color) (left) Experimental geometry for a Corbino spectrometer. (right) The real and imaginary parts $\sigma_1 + i\sigma_2$ of the optical conductivity spectrum of UPd_2Al_3 at temperature T = 2.75 K. The data are fit to $\sigma_{dc}(1 - i\omega\tau)^{-1}$ with $\sigma_{dc} = 1.05 \times 10^5 (\Omega - cm)^{-1}$ and $\tau = 4.8 \times 10^{-11} s$ and show excellent agreement with the Drude prediction. Adapted from (12; 13)

As an example of the power of the technique we show in Fig. 8 (right) recent measurements taken on films of the heavy-fermion compound UPd_2Al_3 at $T = 2.75$ K. The data show almost ideal Drude behavior with a real conductivity of Lorentzian shape and an imaginary conductivity that peaks at the same ω as the real conductivity has decreased by half. The anomalous aspect is the Drude peak is seen to be of remarkably narrow width - almost 500 times narrower than that of a good metal like copper. This is a consequence of the mass renormalizations in the heavy fermion compounds and a feature that would have been completely undetectable with a conventional spectrometer.

Recently there also been the very interesting development of a bolometric technique for high-resolution broadband microwave measurements of ultra-low-loss samples, like superconductors and good metals (18). This technique is a non-resonant one where the sample itself is actually used as a detector in a bolometric fashion. Microwaves are fed through a rectangular coaxial transmission line into which the sample under test and a reference sample are mounted. Small changes in the sample and reference's temperature are monitored as they absorb microwave radiation. The key to the success of this technique is the *in situ* use of this normal metal reference sample which calibrates the absolute microwave incident power. As the absorbed power is proportional to the surface resistance $R_s(\omega)$, the independent measure of the incident power allows one to measure the surface resistance precisely.

In such an apparatus, the sample temperature can be controlled independently of the 1.2 K liquid-helium bath, allowing for measurements of the temperature evolution of the absorption. The minimum detectable power of this method at 1.3 K is 1.5 pW, which corresponds to a surface resistance sensitivity of $\approx 1\mu\Omega$ for a typical $1mm \times 1mm$ platelet sample. The technique allows very sensitive measurements of the microwave surface resistance over a continuous frequency range on highly con-

ducting samples. This is a region of sample impedances generally inaccesible with the Corbino technique and only available at discrete frequencies in microwave cavities.

A disadvantage of the technique is that although one measures $R_s(\omega)$ the quantity of interest is typically the complex conductivity $\sigma(\omega)$. One must make various assumptions to get this from the relation for surface impedance

$$Z_s = R_s + iX_s = \sqrt{\frac{i\omega\mu_0}{\sigma_1 + i\sigma_2}}. \quad (45)$$

as X_s is not measured. At low temperatures and frequencies in the superconducting state σ_2 is mostly determined by the superconducting response and can be related to the independently measured penetration depth λ. σ_1 then follows from the relation $R_s = \frac{1}{2}\mu_0^2\omega^2\lambda^3\sigma_1$. At higher temperatures and frequencies a more complicated iterative procedure must be used that is based on the Kramers-Kronig transform (18).

This technique has been used to measure the real part of the conductivity of $YBa_2Cu_3O_{6.5}$ single crystals across a wide frequency range as shown in Fig. 9. One can see a quasi-Drude like peak at low frequencies that comes from quasi-particle excitation at the nodes of the *d*-wave superconductor. The peak has a narrow width of the order of 5 GHz, signifying a collapse of quasiparticle scattering in the superconducting state and very long quasiparticle scattering lengths. This is indicative of the very high quality of these $YBa_2Cu_3O_{6.5}$ single crystals. Measurements of a broadband nature on these kind of materials are not possible with other techniques. As powerful as it is, the technique is hampered by the fact that various assumption must be made about σ_2. This is problematic for materials where its dependence is not known *a priori*.

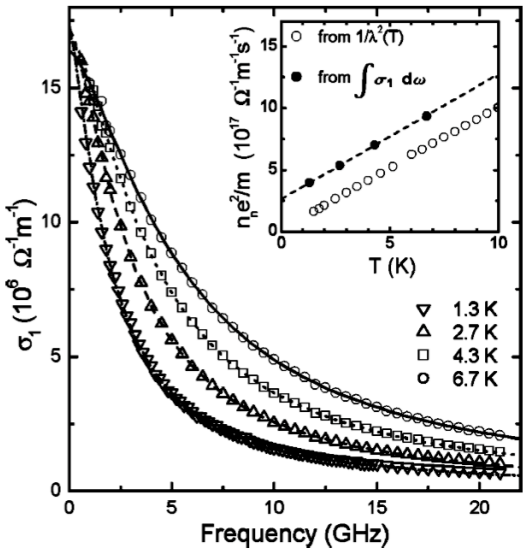

FIG. 9 The real part of the microwave conductivity $\sigma_1(\omega)$ extracted from measurements of $R_s(\omega)$ as described in the text and Ref. (18). Figure adapted from (18).

B. THz spectroscopy

Time scales in the picosecond (10^{-12} sec) range are among the most ubiquitous in condensed matter systems. For example, the resonant period of electrons in semiconductors and their nanostructures, the scattering times of electrons in metals, vibrational frequencies of molecular crystals, superconducting gap energies, the lifetime of biologically important collective vibrations of proteins, and - now - even the transit time for an electron in Intel's new THz transistor - these are all picosecond phenomena. This ubiquity means that experimental probes employing Terahertz (THz) electromagnetic radiation are potentially quite powerful. It is unfortunate then that this spectral range lies in the so-called 'Terahertz Gap' - above the capabilities of traditional electronics and the microwave range, but below that of typical optical instrumentation. In recent years, however, there have been a number of developments that allow measurements in the THz range in a manner that was not previously accesible. These come in the form of time domain THz spectroscopy and the increasing use of Backward Wave Oscillator (BWO) based spectrometers.

As mentioned, the THz spectral region has been a traditionally difficult part of the electromagnetic spectrum to work in. This has been for a number of reasons including weak sources, long wavelengths, and contamination by ambient room temperature black body radiation. In recent years, however, a number of dramatic technical advances such as *time-domain* THz spectroscopy (TDTS) using so-called 'Auston' switch generators and detectors have enabled measurements that span this gap in measurement possibilitites. As such, THz spectroscopy has become a tremendous growth field (19), finding use in a multitude of areas including characterization for novel solid-state materials (20; 21), optimization of the electromagnetic response of new coatings (22), probes of superconductor properties (23; 24), security applications for explosives and biohazard detection (25), detection of protein conformational changes (26), and non-invasive structural and medical imaging (27–29).

TDTS works (See Ref. (30) for an additional excellent short summary) by the excitation of a source and activation of a detector by ultrafast femtosecond laser (typically Ti-sapphire) pulses. A basic schematic is shown in Fig. 10. A femtosecond laser has, *via* a beam splitter, its radiation split off to fall on source and detector Auston switches, which are typically pieces of Low Temperature-GaAs with two electrodes grown on top in a dipole arrangement and separated by approximately 20 μm (Fig. 11). Before laser illumination, the switch has a resistance of a few megaohms. After the fast illumination by the femtosecond laser pulse, the source switch's resistance falls to a few hundred ohms and with a bias by a few tens of volts, charge carriers are acceler-

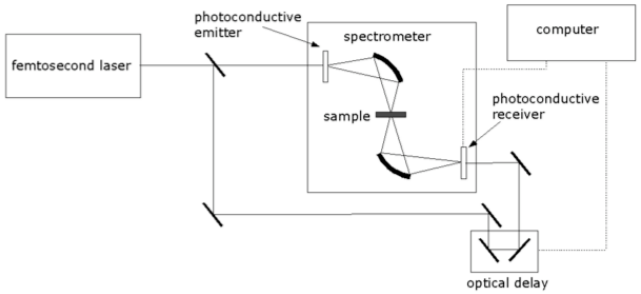

FIG. 10 A diagram of a typical experimental layout used in TDTS.

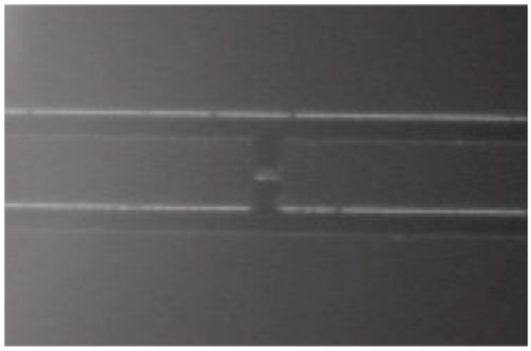

FIG. 11 An optical image of the two-contact photoconductive 'Auston' switch antenna structure used in TDTS. Two electrodes are grown on top of an insulating high defect semiconductor, like low temperature grown GaAs or radiation damaged silicon. Electrode spacing is typically on the order of microns.

ated across the gap on a time scale of a few picoseconds. Their acceleration produces a pulse of almost single-cycle radiation, which then propagates through free space and - collimated by mirrors and lenses - interacts with the sample. Measurements have been typically performed in transmission. After passing through the sample, THz radiation falls on the second Auston switch, which is also activated by the femtosecond pulse. Whereas the first Auston switch was DC biased, the 2nd Auston switch is biased by the electric field of the THz radiation falling upon it. Current flows across the second switch with the direction and magnitude proportional to this transient electric field at the instant the short femtosecond pulse impinges on it. The experimental signal is proportional to this current with a magnitude and polarity that reflects the THz electric field at the switch. A delay line is then advanced and the THz electric field at a different time can be measured. In this way, the entire electric field profile as a function of time can be mapped out as shown in Fig. 12(left). The time-domain pulse is then Fourier transformed to get the complex electric field as a function of frequency. A reference measurement is also performed on an aperture with no sample. The measured transmission function is the ratio of the signal transmission to the reference [Fig. 12(right)].

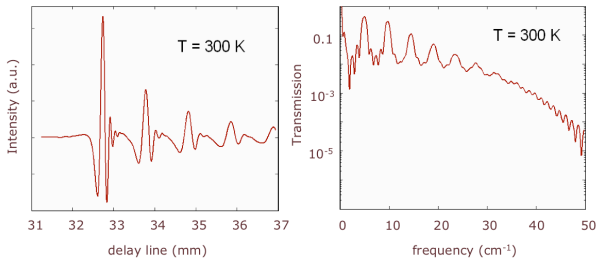

FIG. 12 (Color) (left) Time-domain trace of electric field transmission through 60 μm thick $SrTiO_3$ subtrate. Multiple reflections from front and back surfaces are readily visible. (right) Power spectrum of the transmission through the same 60 μm thick $SrTiO_3$ subtrate. The data is obtained from the squared Fourier transform of the data in (left) and ratioed to a reference aperature signal. From (31)

There are a number of unique aspects to TDTS that allow it to work exceptionally. Since the detected signal is proportional to the instantaneous electric field, and not the power, the measured transmission function is the *complex* transmission coefficient for the *electric field*. This allows one to invert the data directly to get the real and imaginary optical constants (e.g. the complex conductivity) of the material. This is essential for a thorough characterization of material's properties. Typical optical measurements discussed below measure only reflected or transmitted power, quantities in which the complex optical constants of interest are confolded into in a non trivial fashion. In such measurements one has to measure over the largest frequency range possible (even if one is only interested in a limited spectral range), extrapolate to both DC and infinite frequency, and then Kramers-Kronig transform to get phase information. In TDTS one gets both components by direct inversion.

TDTS is also capable of unprecedentedly high signal-to-noise ratios. Typically efforts in the THz and far infrared spectral range are complicated by a very large ambient black body radiation background. In the case of TDTS the fact that the signal is 'time-gated' and coherent, whereas black-body radiation is incoherent, allows a very high detection efficiency. Additionally, since the detected quantity is actually electric field and not power (proportional to electric field squared), the noise in the spectral power is reduced by a factor proportional to the electric field itself. These aspects allow detection of transmission signals approaching one part in 10^6. This is an incredibly large dynamic range and is essentially unprecedented in optically based spectroscopies where one part in 10^3 is typically considered extremely good.

The other major development for THz spectroscopy is the increased use of Backward Wave Oscillators (BWOs) Although developed in the 60's, BWOs are gaining increasing prominence in the investigation of correlated systems in the important THz range (32). These BWOs are traveling wave guide tubes, capable of producing very

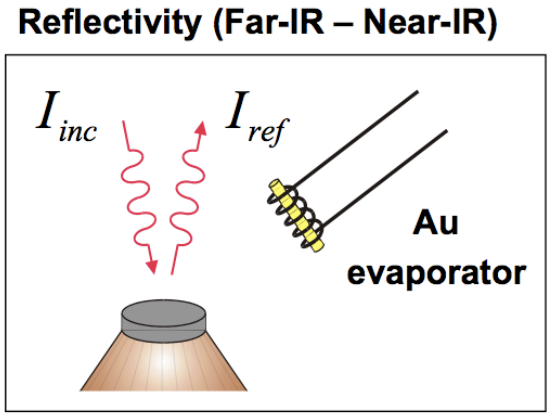

FIG. 13 Absolute reflectivity $R(\omega)$ is obtained by measuring the reflected intensity and ratioing with the intensity after gold evaporation. Figure courtesy of A. Kuzmenko.

monochromatic THz range radiation over a relatively broad range per device. With a number of tubes, it is unique method to cover the 0.03 THz to 1.5 THz range in a continuous wave configuration.

The longer wavelengths in this spectral region give the capabilities to measure phase of transmitted waveforms through Mach-Zender two-beam polarization interferometry. This method also allows direct precision measurements of both real and imaginary components of the complex optical response without resort to Kramers-Kronig transforms and their associated ambiguities. A spectrometer based on BWOs is easily integrated with a low temperature cryostat and magnetic field system as well as glove boxes for environmental control.

C. Infrared

Fourier transform infrared reflectivity (FTIR) is the workhorse spectroscopy of optical measurements (Fig. 14). Measurements are possible from $\sim$ 10 cm^{-1} to approximately 25,000 cm^{-1}, although measurement get increasingly difficult below 50 cm^{-1}. Heroic efforts can push the lower end of this range slightly below 10 cm^{-1} (33). Here the quantity of interest is typically the power reflectivity (transmission measurements are possible as well). One shines broadband light, sometimes from several different sources, on a sample surface and *via* an interference technique measures the reflected intensity. As the source spectrum and detector response can have all kinds of frequency structure, it is necessary to reference the reflected signal against a standard sample to obtain the absolute reflectivity. Typically the reference spectrum is chosen to be a noble metal like gold whose reflectance can to good approximation be taken to be unity over a broad frequency region below the material's plasma frequency (see below). Typically gold is evaporated onto a sample as shown in Fig. 13 or the sample is replaced with a mirror to do this referencing.

As the materials we are interested in typically have interesting experimental signatures in both the real and imaginary response, it is not sufficient to to compare to theory by simply measuring quantities like *absorbence*. We want quantities like the complex conductivity or dielectric function. It is not necessarily straightfoward to obtain a complex quantity from the measured scalar magnitude of the reflectivity $R(\omega)$. Unlike TDTS, phase is not measured in FTIR measurements. Therefore typically use is made of the above discussed Kramers-Kronig transforms, which apply to any causal response function. If one knows one component of the response (real or imaginary) for all frequencies then one can determine the other component. For reflected power, one can obtain the phase shift as

$$\phi(\omega) = -\frac{1}{\pi} P \int_{-\infty}^{\infty} d\omega \frac{ln|R(\omega)|}{\omega' - \omega}. \tag{46}$$

Of course the problem is that one doesn't measure over an infinite frequency range. In typical FTIR spectoscopy, the usual mode of operation is therefore to measure over as large a frequency range as possible and then extrapolate with various schemes to $\omega \to 0$ and $\omega \to \infty$. This method works quite well for some materials, although it can generate large errors when, for instance, reflectivities approach unity as they do in good conductors at low frequencies.

As mentioned, FTIR spectoscopy is a standard spectroscopic technique for the characterization of materials and chemicals. It is used routinely to identify the presence of various chemical bonds in chemistry as in, for instance, $C = C$ or $C = O$, which all have distinct frequencies and absorptive strengths. It is also the standard optical tool for probing materials like high-T_c superconductors (34). It has the advantage of being relatively easy to perform and possessing a very large spectra range. It has the above mentioned disadvantage of only measuring a scalar - the power - and having a lower bound on the spectral range that is at the limit of that explicitly relevant for many correlated materials.

D. Visible and Ultraviolet

The technique of optical reflection begin to become more difficult at frequencies on the order of the plasma frequencies of metals. To do reflectivity measurements, one always needs a standard sample. Standard metal references cannot be used above their plasma frequencies as their reflectivity changes quickly with frequency. Quartz or silicon which have an approximately flat (but low) reflectivity can be used as a reference. However, more common nowadays is to use techniques such as ellipsometry to determine complex optical coefficients in this spectral range.

Ellipsometry is an optical technique for determining properties of surfaces and thin films. Although the

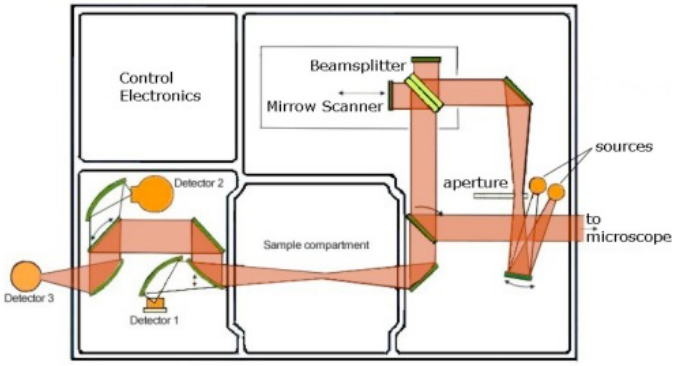

FIG. 14 (Color) Modified Fourier Transform Spectrometer Bruker 66. As shown, the spectrometer is setup to perform reflection, but with additional mirrors near-normal incidence reflection is possibe. The apparatus works by shining broad band light from a variety of sources on a sample. Reflected or transmitted intensity is measured at a few different detectors. A beamsplitter/interferometer apparatus allows the resolution of distinct frequency components. Figure from `http://www.pi1.physik.uni-stuttgart.de/research/Methoden/FTIR_e.php`. Courtesy of N. Drichko.

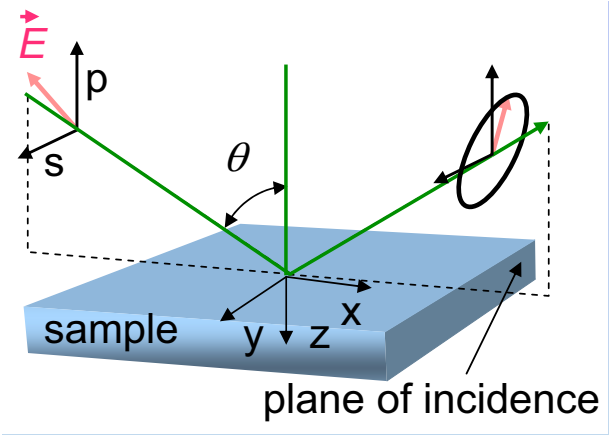

FIG. 15 (Color) Schematic showing the basic principle of ellipsometry. Glancing incidence light linearly polarized with both s and p components is reflected with different intensities and a relative phase shift. A characterization of the resulting elliptically polarized reflected light's minor and major axes, as well as tilt angle gives a unique contribution of the complex optical constants of the material.

method was originally used as far back as 1887 by Paul Drude to determine the dielectric function of various metals and dielectrics, it only gained regular use as a characterization tool in the 1970s (35; 36). It is now widely used in the near infrared (NIR) through ultraviolet (UV) frequency ranges in semiconductor processing for dielectric and thickness characterization.

When linearly polarized light is reflected from a surface at glancing incidence the in- (p) and out-of-plane (s) of incidence light is reflected at different intensities as well as suffering a relative phase shift. The reflected light becomes elliptically polarized as shown in Fig. 15. The shape and orientation of the ellipse depend on the angle of incidence, the initial polarization direction, and of course the reflection properties of the surface. An ellipsometer measures the change in the light's polarization state and characterizes the *complex* ratio ρ of the in- (r_p) and out-of-plane (r_s) of incidence reflectivities. The Fresnel equations allow this quantity to be directly related to various intrinsic material parameters, such as complex dielectric constant or layer thicknesses.

The ellipsometer itself is designed to measure the change in polarization state of the light reflected from a surface at glancing incidence. From a knowledge of the orientation and polarization direction of the incident light one can calculate the relative phase difference, Δ, and the relative amplitude difference, ($\tan\Psi$), between the two polarization components that are introduced by reflection from the surface.

Given the *complex* ratio ρ of the in- (r_p) and out-of-plane reflectivities (r_s), various intrinsic material parameters can be generated *via* the Fresnel equations. For instance, in a homogeneous sample the complex dielectric constant $\epsilon = \epsilon_1 + i\epsilon_2$ is related to ρ as given in Eqs. 47, 48 and 49 below. Here as usual ϵ_1 parameterizes the polarizability of a material, whereas ϵ_2 parameterizes the dissipative properties. Here, ϵ_z is the complex dielectric constant perpendicular to the reflection surface and ϵ_x is the complex dielectric constant in the plane of the reflection surface, and θ is the angle of incidence as shown in Fig. 15.

$$\rho = r_p/r_s = \tan\Psi e^{i\Delta}, \tag{47}$$

$$r_p = \frac{\sqrt{1-\epsilon_z^{-1}\sin^2\theta} - \sqrt{\epsilon_x}\cos\theta}{\sqrt{1-\epsilon_z^{-1}\sin^2\theta} + \sqrt{\epsilon_x}\cos\theta}, \tag{48}$$

$$r_s = \frac{\cos\theta - \sqrt{\epsilon_y - \sin^2\theta}}{\cos\theta + \sqrt{\epsilon_y - \sin^2\theta}}. \tag{49}$$

In a typical configuration, monochromatic light is incident on a glancing trajectory θ close to the Brewster angle (usually $\sim 65-85°$ for bad metals at high frequencies) with a linear polarization state of 45°. As the typical detector measures power and not electric field, it is essential that the light's elliptical polarization is measured over at least 180° (and more typically 360°). To completely characterize the phase, it is clearly *not* sufficient to simply measure the projection of the ellipse along two orthogonal directions, as can be seen by construction in Fig. 16. In order to get the phase information, the ellipse's orientation and major and minor axes must be known. Generically, the light originally linearly polarized at 45° is changed to an elliptical polarization with

its major axis displaced from 45°. A characterization of this ellipse's major and minor axes, as well as tilt angle is a direct measure of the complex amplitude reflection coefficients, which can then be related to intrinsic material quantities.

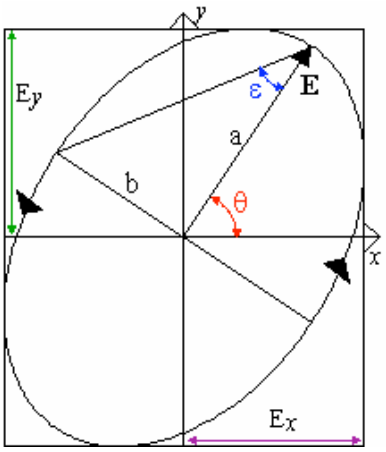

FIG. 16 (Color) To completely characterize the electric field vectors and their phase, it is insufficient to measure the projection of the ellipse along two orthogonal directions. The complete ellipse must be mapped out to get its major and minor axes and tilt angle.

The fact that ellipsometry measures the ratio of two simultaneously measured values gives it several distinct advantages as a characterization tool over simple reflectivity. It is highly accurate and reproducible even at low intensities as many systematic errors are divided out. Moreover, unlike reflectivity measurements, the technique is self-normalizing and a reference sample is not necessary. This is important as the choice of a reference can be problematic in the optical and ultra violet spectral range or when the surface is of unknown quality. The method is also particularly insusceptible to source intensity fluctuations as they are also divided out. Perhaps most important for the overall utility of the technique is that the method also measures a phase, which gives additional information regarding materials properties. The phase information can also be used to generate the *complex* optical constants (the complex dielectric constant for instance, or the complex index of refraction n and k or the complex conductivity σ) which is essential information for a complete characterization of a material's optical response. If the optical constants are known, the phase information can be used to sensitively measure films thicknesses. As mentioned above, the technique is well established and widely used in the NIR through ultraviolet (UV) frequency ranges (37; 38). There have been a number of attempts to extend ellipsometry to these lower frequencies (37–39), but among other reasons the lack of sufficiently intense sources has meant that such efforts have met with limited success, although synchrotron based efforts have had some success in this regard (40). If ellipsometry has a disadvantage it is that with typical grating monochromator data acquisition (i.e. one frequency stepped at a time) it is relatively slow as both the grating and polarizers must continue to be moved. In such a setup one loses the rapid acquisition time of the multiple frequency multiplexing in, for instance, Fourier transform infrared reflectivity (FTIR).

The energy scales of the visible and ultraviolet, which are measured by ellipsometry are not usually explicitly relevant for strongly correlated systems. Typically we are interested in much lower energies that are on the order of the temperatures that phenomena are expressed. However, such energies are relevant for the determination of important band structure parameters on, say, 3D materials that photoemission cannot be performed on. Characterization of materials in this range is also imperative to constrain the phase information at low energies when performing Kramers-Kronig with reflectivity data. Recently an extremely powerful method for combining different data sets using a Kramers-Kronig consistent variational fitting procedure was developed (41). It allows a general procedure for combining say, DC resistance, cavity microwave measurements at a few distinct frequencies, IR power reflectivity, and ellipsometry to extract over a broad energy range of all the significant frequency and temperature dependent optical properties.

IV. EXAMPLES

A. Simple Metals

Noble metals like silver and gold provide a good first step for the understanding the electrodynamics of solids. Compare the reflection spectra of silver and gold given in Fig. 17 as a function of energy. The reflection spectra of silver shows a sharp plasma edge around 3.8 eV Gold has a much lower plasma frequency with its plasma edge at a wavelength of around 2.5 eV. Also shown is the reflection spectra for aluminum which has a much larger plasma frequency than any of these at around 15.5 eV. The small dip in Al around 1.65 eV is caused by an interband absorption and is not its plasma frequency.

From these spectra we can immediately see the reason for the visual difference between silver and gold. As mentioned above, the reflection/transmission properties of metals greatly change above their plasma frequencies. If not for the presence of interband transitions, metals would be transparent in this regime. The lower plasma frequency of gold is what determines its yellowish color in reflection. It reflects less in the blue/violet portion of the spectra and hence looks yellowish. In contrast the plasma frequency of silver is in the UV range and so the reflection of silver is almost constant at constant throughout the infrared to visible range. Aluminum's plasma frequency is higher yet still and so the major differences in its optical properties as compared to silver are invisible to the human eye.

As discussed above, within the Drude model the

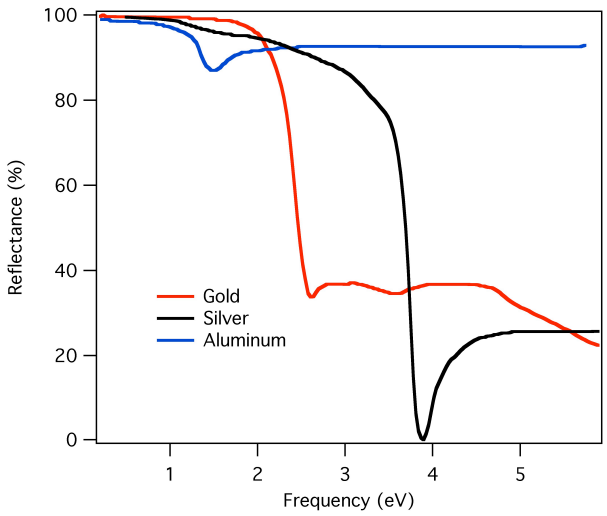

FIG. 17 Reflectance curves for aluminium (Al), silver (Ag), and gold (Au) metal at normal incidence as a function of incident energy. The plasma frequencies of silver and gold are clearly seen. The small dip in aluminum's curve around 1.65 eV is caused by an interband absorption and is not its plasma frequency. Aluminum's plasma frequency lies at much higher energies at around 15.5 eV. Adapted from Ref. (42).

plasma frequency is set by $\omega_p = \sqrt{\frac{4\pi Ne^2}{m}}$. This is frequency of the dip in the plasma frequency, the zero crossing in ϵ_1, and the frequency of free longitudinal charge oscillations (the *plasmon* frequency). However, the presence of interband excitations, which contribute a high frequency dielectric constant ϵ_∞ changes the situation. The features are now exhibited at the so-called *screened* plasma frequency set by $\tilde{\omega_p} = \sqrt{\frac{4\pi Ne^2}{\epsilon_\infty m}}$. It is interesting to note that the carrier density and masses of silver and gold are almost identical and so the difference in their plasma frequencies comes from the renormalization effect of the interband transitions ϵ_∞.

Data like that shown in Fig. 17 can, with appropriate extrapolations to high and low frequency, be Kramers-Kronig transformed to get the real and imaginary dielectric function as shown in Fig. 18 for silver and gold. As expected they both show strong almost perfect $\omega = 0$ Lorentzian Drude peaks of almost equal weight, but gold shows stronger interband absorptions, gives it a larger ϵ_∞ that renormalizes its plasma frequency. Such spectra can be decomposed into various contributions as shown in Fig. 19 for gold. Also as expected there is a strong zero frequency Drude peak contribution as well as interband contributions. Although the interband piece shows some resemblance to the Drude-Lorentz plots in Fig. 6, the shape is a more rounded cusp, which is characteristic of transitions within the manifold of d-electron states.

In Fig. 20 a similar plot of the complex response functions for Aluminum is shown. In addition to the metallic $\omega = 0$ Lorentzian Drude peak, the prominent absorption

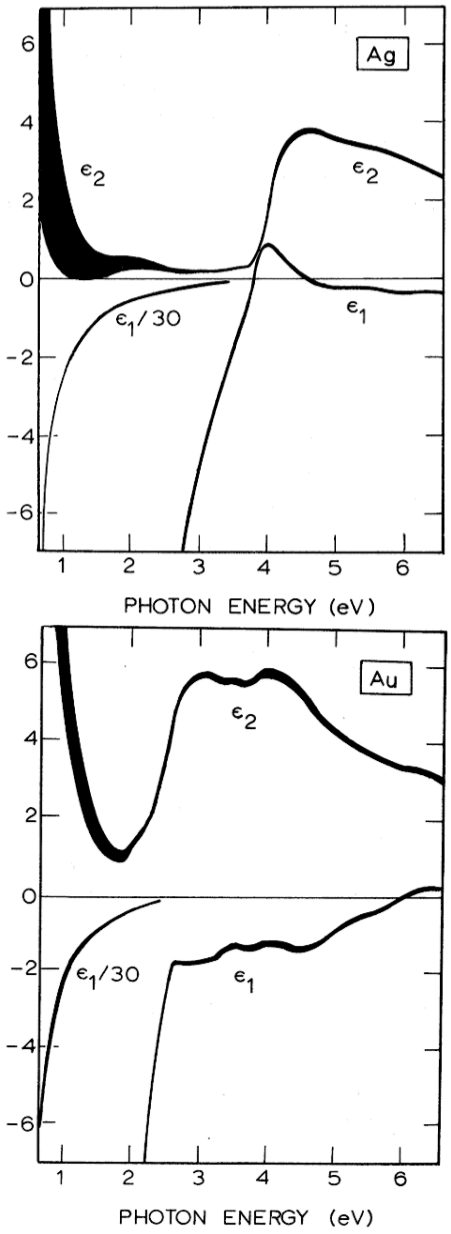

FIG. 18 Real and imaginary dielectric functions for silver (top) and gold (bottom). The thickness of the curve indicates the experimental uncertainty, which originates mainly in the Kramers-Kroning transform. From Ref. (43).

that gives the dip in the reflectivity curve around 1.65 eV can be clearly seen. That this dip in the reflectivity does not reflect the plasma frequency can be see in the plot of the loss function Im $-\frac{1}{\epsilon}$, which shows a strong peak at the 'screened' plasma frequency 15.5 eV (i.e. the zero cross of ϵ_1.

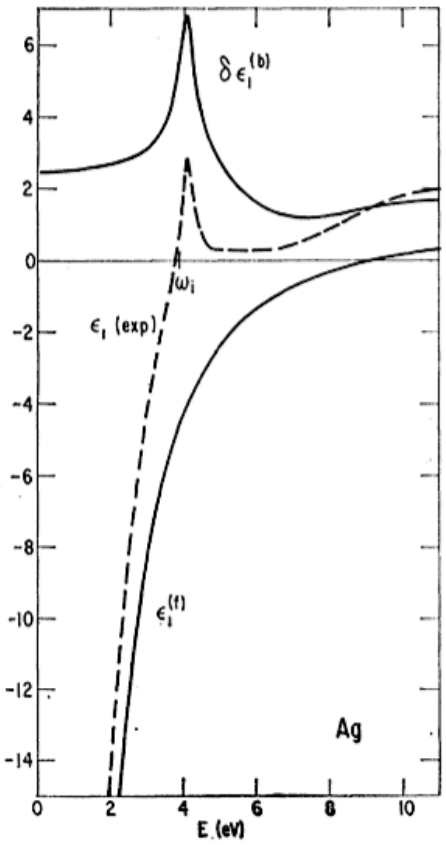

FIG. 19 Decomposition of the dielectric function of gold into Drude and interband contributions. The threshold absorption for interband excitations is indicated by ω_i. $\epsilon_1^{(1)}$ is the Drude contribution. $\delta\epsilon_1$ is the interband piece. From Ref. (45).

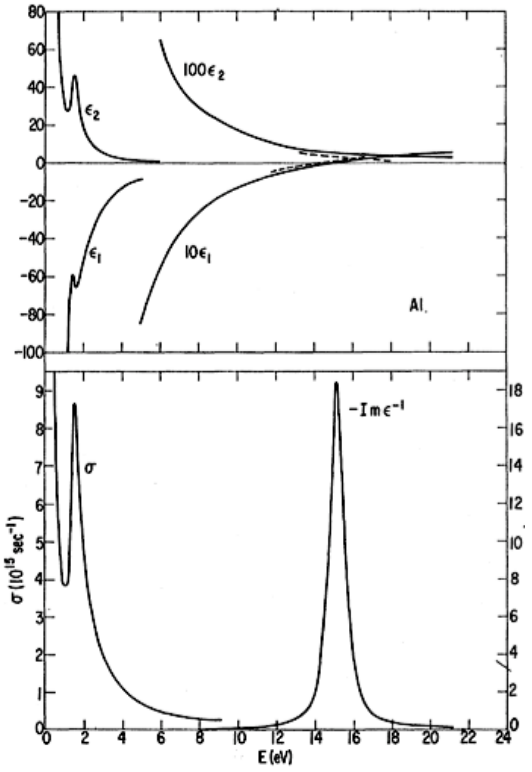

FIG. 20 (top) Real and imaginary dielectric functions for aluminum. (bottom) Real part of the conductivity and the loss function. In addition to the Drude peak, a prominent absorption is found around 1.65. This feature gives the dip in the reflectivity curve around the save energy. The loss function shows a strong peak at the screened plasma frequency 15.5 eV. From Ref. (44).

B. Semiconductors and Band Insulators

In semiconductors and band insulators, the real part of the conductivity is dominated by interband transitions (red in Fig. 2). At low temperatures in a clean undoped insulator, naively one expects to see a gap with no conductivity and then a sudden onset at the gap edge. In fact, various other contributions are also possible inside the gap. Electron-hole pair bound states can form as excitons and give dissipative response and be seen as sharp peaks below the gap. This is seen for instance in Fig. 21 for the ionic insulator KCl, where the only electronic transition in addition to the band edge excitation is a series of below gap excitons. Even lower frequencies than those shown would reveal a series of sharp peaks from phonons down in the 50 meV range.

If one starts to dope into a typical semiconductor like phosphorus into silicon, massive changes in the optical spectra occur. At very low doping levels one can discern the sharp absorptions of individual donors as seen in the bottom of Fig. 22. As the dopant density is increased inter-pair and inter-cluster quantum tunneling broadens the spectra until a prominent a prominent impurity band forms in the gap as shown in Fig. 23. Charge transitions can occur in this manifold of impurity states. Below a certain critical doping such a doped state is an insulator and called an *electronic glass*. I discuss this state of matter below.

C. Electron glasses

Many crystalline and amorphous semiconductors show a metal-insulator transition (MIT) as a function of dopant concentration or stochiometry. On the insulating side of the transition, the materials are insulators not due to completely filled bands (as in the case of a band insulator) or interactions (as in the case of a Mott insulator), but because electronic states at the chemical potential are localized due to disorder. Such materials which have a random spatial distribution of localized charges have been called - in analogy with structural glasses - *electron-glasses* and are more generally termed Anderson insulators.

At finite temperatures these materials conduct under DC bias *via* thermally activated transport of charges

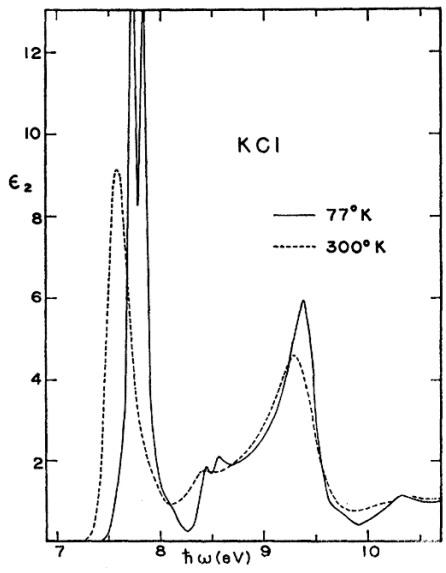

FIG. 21 Imaginary dielectric function of KCl. The absorption around 9 eV is the bad gap. The series of sharp features at energies below the band gap are due to excitons. From Ref. (46)

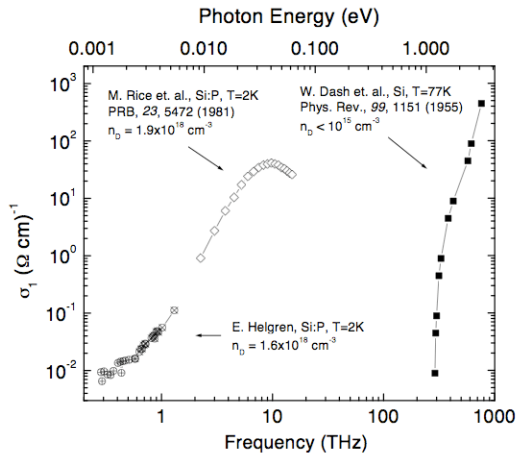

FIG. 23 Optical conductivity of silicon doped close to the 3D metal-insulator transition. The optical band gap is visible *via* the high energy onset at 1.12eV. The intermediate energy conductivity is associated with excitations from the dopant band to the conduction band. The conductivity at the lowest energies, i.e. photon assisted hopping conductivity, is due to intra-dopant band excitations. From Ref. (49).

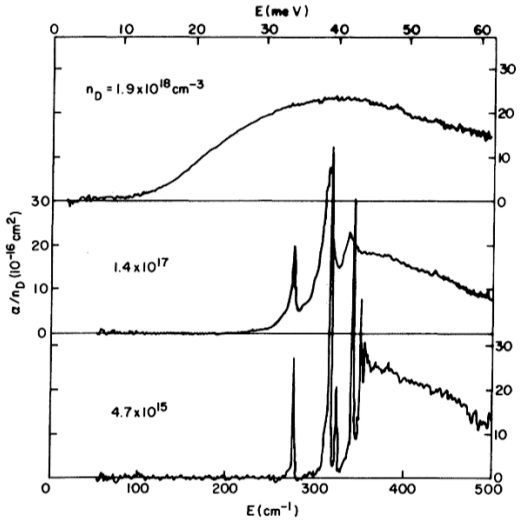

FIG. 22 Absorption coefficient in P doped Si normalized to the number of donors n_D for the three different labeled doping levels at 2 K. At the lowest doping, absorptions due to individual donor atoms can be seen. These absorption broaden into a impurity band at higher dopings. The direct gap is at much higher energies as shown in Fig. 23. From Ref. (47)

hopping between localized states in the impurity band. The DC conductivity tends to zero as the temperature tends to zero. However, because their insulating nature derives from localization of the electronic orbitals and not necessarily a vanishing density of states at E_F, such materials can have appreciable conductivity at low frequency deriving from transitions between localized states inside the impurity band. Although electron transport in electronic glasses is still not completely understood, different regimes for AC transport can be distinguished depending on the strength of electron-electron interactions, the energy scale being probed and the amount of disorder. See Helgren *et al.* (49) for a complete discussion on this subject.

Far away from the MIT and in regimes when electron-electron interactions are not significant, one considers a so-called Fermi glass. This is an ensemble of localized charges whose properties are primarily determined by the Fermi statistics. When the long-range Coulomb interaction is of the same order as the disorder potentials, a so-called Coulomb glass emerges, and finally, near the transition to the metallic state, fluctuations lead to a quantum critical regime. For these various regimes, certain characteristic power law and exponential functional forms for the AC and DC transport are expected. For instance, in a Fermi glass the AC conductivity is expected to be a power law $\sigma \propto \omega^2$ (50). In a Coulomb glass the conductivity is expected to take the form $\sigma \propto U(r)\cdot\omega+\omega^2$ (51). Here, the non-interacting Fermi glass functional form is returned at high frequencies, but a linear dependence is found at low frequencies. The crossover between these regimes is smooth and set by $U(r)$ which is the typical long range interaction strength between the charges forming the absorbing resonant pair. There are expected to be logarithmic corrections to these power laws. As the energy scale $U(r)$ characterizes the long range Coulomb interaction, it is expected to go to zero at the MIT. As one approaches the quantum critical point, the behavior may also be interpreted using scaling laws (discussed below) that connect the temperature, frequency and concentra-

tion dependence of the response. It is expected that there is a correspondence between the frequency and temperature dependent conductivity on both sides of the critical concentration. Such an analysis of the conductivity leads to a universal scaling function and defines critical exponents as discussed below.

In Fig. 24, the pioneering data of Stutzmann and Lee (17) on Si:B demonstrates the real part of the conductivity measured with a broad band microwave Corbino spectrometer. The data shows a remarkable observation of conductivity linear in frequency at low frequencies and a sharp crossover at $U(r)$ to ω^2 at high frequencies. Work on Si:P on samples farther from the metal-insulator transition shows the same behavior (48; 49), albeit the energy scale of the crossover is found at higher energies as it is set by the long range Coulomb interactions (which increases away from the MIT). Although the proposed functional form of Efros and Shkovlkii approximately fits the data of Stutzmann and Lee (17) (and of Helgren *et al.* (48)), it fails to account for the very sharp crossover between power laws. Stutzmann and Lee (17) interpreted the sharp crossover as deriving from a sharp feature in the density of states - the Coulomb gap (a depression at the Fermi energy in the density of states that is a consequence of the long range Coulomb interaction). However, such an interpretation is at odds with theory and moreover, was not consistent with the work of Helgren *et al.* (48), where it was shown that the crossover was set by the typical interaction strength. The sharp transition between power laws remains unexplained; although one should consider that this sharp crossover may arise from collective effects in electron motion (53).

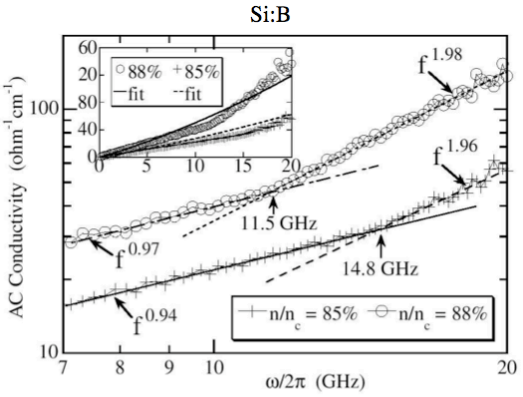

FIG. 24 The real part of the complex frequency dependent conductivity for two samples of Si:B at 85%and 88% of the way to metal-insulator transition (17). Data has been measured up to 20 GHz with a Corbino geometry microwave probe. The crossover in the frequency dependent conductivity from linear to quadratic is qualitatively consistent with a crossover from Coulomb glass to Fermi glass behavior.

The theoretical functional form and experimental observation is remarkable, because the ordering of regimes is at odds with the typical situation in solid state physics. Typically it is that non-interacting functional forms are expected at low frequency and temperature, while the explicit effects of interactions are seen at higher frequencies. The canonical example of this ordering is the Fermi liquid, where it is the low frequency spectra which can be typically modeled in terms of quasi-free non-interacting particles (perhaps with renormalized masses). The higher energy spectra are typically more complicated and show the non-trivial effects of electron-electron and electron-boson interactions. Similar physics is exhibited in the heavy-fermion compounds in that it is the low frequency regime that can be understood in terms of conventional Boltzmann transport of heavy electrons. In contrast, in electron glasses, it is the low frequency spectra which shows the effect of interactions while the high frequency spectra returns the non-interacting functional form.

This was not the original expectation. Anderson originally coined the term "Fermi glass" in analogy with the Fermi liquid, to describe a ensemble of localized charges whose properties where largely determined by Fermi statistics alone (54).

> "(The) Fermi liquid theorem is a rigorous consequence of the exclusion principle, it happens because the phase space available for real interactions decreases so rapidly (as E^2 or T^2). The theorem is equally true for the localized case: at sufficiently low temperatures or frequencies the non-interacting theory must be correct, even though the interactions are not particularly small or short range: thus the non-interacting theory is physically correct: the electrons can form a Fermi glass."
>
> - P.W. Anderson, 1970

It is surprising that even in a material as thoroughly studied as doped bulk silicon that there exists no clear consensus as to the ground state and the nature of the low energy excitations at low dopings. It appears however, that Anderson's speculation is not borne out by the experimental situation. The low lying excitations appear fundementally changed by interactions. Of course, existing experiments do not preclude that at even lower energies the Coulomb glass-like behavior will not break down or give way to a different response like a Fermi glass.

D. Mott insulators

Mott insulators differ from band insulators and Anderson insulators in that their insulating effects derive from correlations and not from filled bands or disorder-driven localization. One expects to see very interesting aspects of spectral weight transfer as charges are doped and they eventually become metals.

At half-filling it is believed that such Mott insulators are characterized by upper and lower Hubbard bands, which are split by an energy U which is the energy to doubly occupy a single site. If one wants to occupy a site doubly, one must pay this energy cost U. As will be discussed below the spectral weight $\int \sigma(\omega) d\omega$ is a conserved quantity which depends on the total amount of charge in a system. It is interesting to account for how spectral weight is transfered by doping electrons to such a system (55).

At half-filling, the lower Hubbard band is filled (occupied) and the upper Hubbard band is unfilled. Since every site in the system has one electron, the spectral weight of upper and lower Hubbard bands are equal. Not consider the situation after one dopes a single electron to the upper Hubbard band. The unoccupied spectral weight of the upper Hubbard band reflects the total number of sites which can have an electron added, the lower Hubbard band reflects the total number of sites occupied by a single electron, and the occupied weight of the upper Hubbard band reflects the total number of sites that are doubly occupied. One expects then that doping a single electron transfers a state each from both the upper and lower Hubbard bands as shown in Fig. 25 because doping changes the number sites which are occupied/unoccupied. It is natural to expect that a state is removed from the unoccupied part of the upper Hubbard band as now a state is occupied. However a state is also removed from the occupied part of the lower Hubbard band as its spectral weight quantifies how many electrons sit on singly occupied sites. The occupied weight of the upper Hubbard band is then '2', and the spectral weights of occupied lower Hubbard band and unoccupied upper Hubbard band are both N-1. The situation differs from doping a semiconductor because then doping a single electron into the upper band, only takes that single state from the upper band. There is no transfer of spectral weight across the gap. An intermediate case is expected for the charge-transfer insulators, which the parent compounds of the high T_c superconductors are believed to be. In these compounds a charge transfer band (consisting primarily of O $2p$ states) sits in the gap between upper and lower Hubbard bands and plays the role of an effective lower Hubbard band. The energy to transfer charge from from an oxygen to copper Δ becomes the effective onsite Hubbard U. Issues of spectral weight transfer in Hubbard and charge transfer insulators are discussed more completely in Ref. (55).

In Fig. 26 we show the doping dependence of the room temperature optical conductivity of $La_{2-x}Sr_xCuO_4$. At $x = 0$ the spectra show a clear charge transfer gap of about 1.8 eV. This largely reflects excitations from O $2p^6$ states to Cu $3d^10$. Upon doping with holes, spectral weight is observed to move from the high energies to low in a manner consistent with the picture for the charge transfer/Mott Hubbard insulators in Fig. 25. It is interesting to note that the charge transfer band remains even for samples that have become superconductors and are known to have a large Fermi surface.

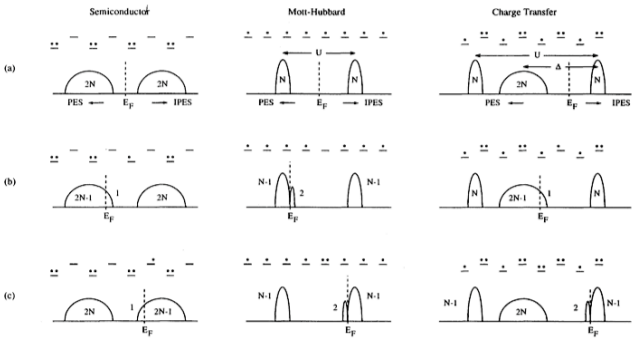

FIG. 25 A schematic of the electron-removal and addition spectra for a simple semiconductor (left), a Mott-Hubbard system in the localized limit (middle) and a charge transfer system in the localized limit. (a) Undoped (half-filled) (b) one-electron doped, and (c) one-hole doped. The onsite repulsion U and the charge-transfer energy Δ are indicated. From Ref. (55)

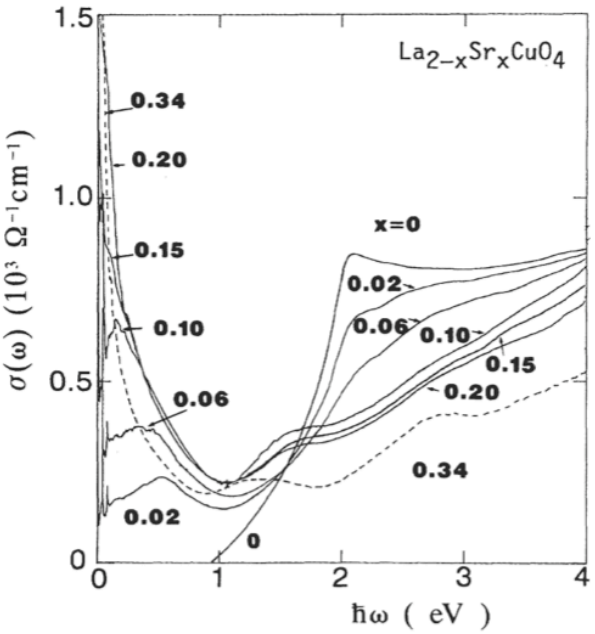

FIG. 26 Doping dependence of the room temperature optical conductivity of $La_{2-x}Sr_xCuO_4$. At $x = 0$ the spectra show a clear charge transfer gap of about 1.8 eV. Upon doping with holes, spectral weight is observed to move from the high energies to low in a manner consistent with Fig. 25. Figure adapted from(56)

.

E. Superconductors and other BCS-like states

One can gain a rough intuition of the electrodynamic response of superconductors for $\hbar\omega \ll 2\Delta$ and T$\ll$T$_c$ from the relations in Eq. 25, which give the dissipationless limit for the Drude model. One expects a δ function peak at zero frequency in the real conductivity and a $1/\omega$ dependence in the imaginary part, whose coefficient is set by the strength of the δ function. At frequencies on the order of the superconducting gap 2Δ, Cooper pairs can be broken and enhanced absorption should be found. At higher temperatures, thermally excited quasiparticles are created and one expects that as they are subject to essentially normal state dissipative processes, they will give a contribution to σ_1 at finite ω.

Very roughly one expects a two fluid scenario where the conductivity is approximately given by $\sigma(\omega) = \frac{\pi}{2}\frac{Ne^2}{m}\delta(\omega=0) + i\frac{N(T)e^2}{m\omega} + \sigma_{1n}(\omega,T)$. At low temperatures, one expects that $N(T)$ is degraded as $1-e^{-\Delta/k_BT}$, as quasiparticles thermally disassociate. As the superfluid density decreases the normal fluid component increases and one may in some circumstances expect an increase in σ_{1n} to go as $e^{-\Delta/k_BT}$.

These above considerations are only approximate however. The explicit temperature dependence of the gap and the mutual screening effects of the superfluid and normal fluid must be taken into account. Among other things, this means that the functional form of the contribution from 'normal' electrons σ_n, although still peaked at $\omega = 0$, will be decidedly non-Lorentzian. Within the context of the BCS theory the response of a superconductor can be calculated from the Mattis-Bardeen formalism. I will not go into the details of the calculation here. Interested readers should consult Tinkham (57). One of the important results from this formalism however is the effect of the superconducting coherence factors, which depending on their sign can lead to enhanced or suppressed absorption over the normal state above or below the gap edge. This means that different symmetries of the superconducting order parameter (or order parameters of other BCS-like condensates like spin- or charge-density waves), leave their signatures on the dissipative response.

Shown in Fig. 27 is the temperature and frequency dependence of the real part of the conductivity σ_1 as evaluated from the Mattis-Bardeen expression for 'type II' coherence factors, which are appropriate for s-wave superconductivity. One can see that at T=0, one has no below gap absorption, and then a gentle rise begins starting at the gap edge 2Δ. Despite the singularity in the density of states, the conductivity is suppressed at the gap edge, as the type I coherence factors effectively cancel the enhanced density of states. As one warms the sample, below gap excitations are possible from thermally excited quasiparticles. Just as above the gap edge the absorption is suppressed, the absorption is enhanced over the normal state at energies below the gap. This is again the consequence of type II coherence factors.

This anomalous behavior is more clear along the temperature axis. If one follows the conductivity at a particular frequency as a function of temperature, one will see a large enhanced absorbence at temperatures below T_c. This result although surprising is direct evidence for coherence effects in the superconductor. An analogous enhancement found in the nuclear relaxation rate *via* NMR - the so-called Hebel-Schlichter peak - was early evidence for the BCS theory (58).

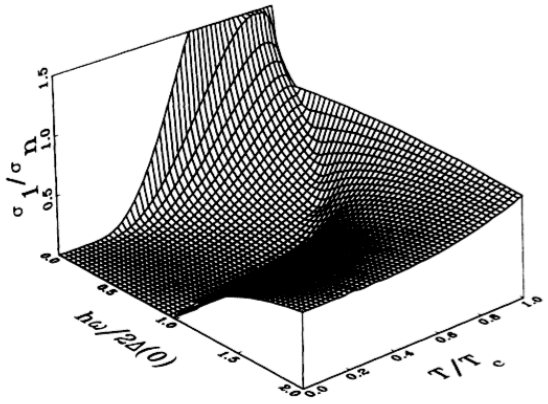

FIG. 27 Temperature and frequency dependence of the conductivity σ_1 as evaluated from the Mattis-Bardeen expression. The coherence peak exists only at low frequencies $\hbar\omega/2\Delta < 0.1$. The cusp in the surface corresponds to the energy gap.

These features contrast with the situation in Type I coherence factors as shown in Fig. 28. In a Type I coherence factor SDW material one expects a very different response. There the coherence factors don't cancel the singularity in the density of states. Likewise, there is no Hebel-Schlicter like peak in the temperature dependence.

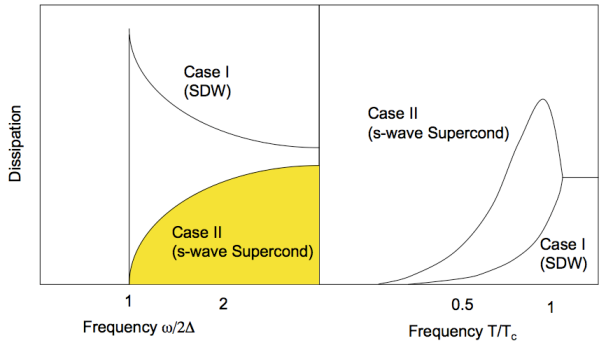

FIG. 28 (Color) (left) Approximate frequency dependence of the dissipation rate from the Mattis-Bardeen theory for Type I and Type II coherence factors. (right) Approximate temperature dependence of the dissipation rate for $\omega = 0.1\Delta$ for both coherence factors.

Qualitatively the behavior for Type II coherence factors is realized in conventional *s*-wave superconductors. In Fig. 29, the normal state normalized conductivity

from some of the original measurements of Palmer and Tinkham (59) is shown, which is in good agreement with the Mattis-Bardeen prediction. The suppression at the gap edge is consistent with type II coherence factors and hence a s-wave superconducting state. Mattis-Bardeen predicts that subgap absorptions rise with increasing temperature and become enhanced over the normal state conductivity.

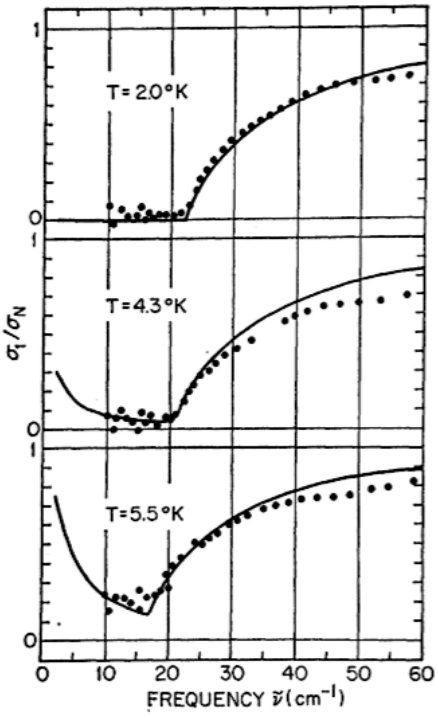

FIG. 29 Frequency dependence of the normalized conductivity through lead films at three different temperatures. The results are obtained through a combination of reflection and transmission measurements. The solid line is a calculation using the Mattis-Bardeen theory with a $2\Delta/\hbar = 22.5$ cm^{-1}. T_c for these lead films is 7.2 ± 0.2 K. From Ref. (59).

In Fig. 30 the conductivity of Nb at 60 GHz as measured in a microwave resonance cavity is shown as a function of temperature (60). The peak below T_c is the electromagnetic equivalent of the Hebel-Schlicter peak in NMR. This is again consistent with s-wave superconductivity.

As noted, different behavior is expected for type I coherence factors. There one expects an absorption enhancehment at the gap edge and no 'Hebel-Schlicter' peak. The lack of such a peak in electromagnetic absorption of cuprate superconductors is at least partial evidence for d-wave superconductivity in those compounds. It is due in part to the lack of a strong singularity in the d-wave density of states, but also because the coherence factor vanishes for $q = \pi, \pi$ since $\Delta_k = -\Delta_{k+\pi,\pi}$. Such data is shown in Fig. 31 where the conductivity measured at a number of different frequencies in the GHz range on

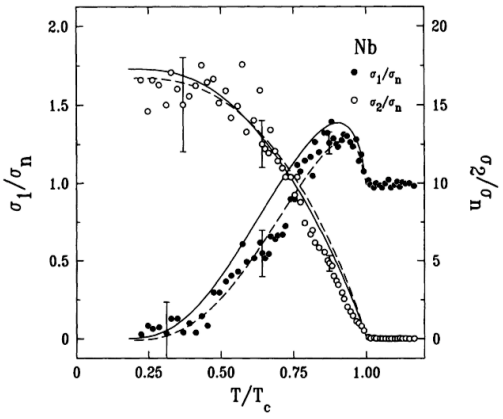

FIG. 30 Temperature dependence of the complex conductivity $\sigma(\omega)$ of Nb as evaluated from surface impedance measurements at 60 GHz in cavities. The solid curve is the weak coupling Mattis-Bardeen prediction. The dashed curve is a strong coupling Eliashberg prediction. From Ref. (60).

YBCO is displayed as a function of temperature (61). The data does show a number of broad peaks in σ_1 at around approximately 35 K, but a comparison with the Mattis-Bardeen prediction shows that it is incapable of describing it as the rise in σ_1 is much more gradual than predicted. An explicit comparison is shown in Fig. 32. This peak has been quite reasonably described in terms of a collapsing scattering rate below T_c of quasiparticles whose number remains appreciable until low temperatures due to the d-wave nature of this compound. An examination of the Drude model shows that in general one expects a peak in σ_1 when the probe frequency is approximately equal to $1/\tau$ the scattering rate. The exhibited peak is therefore not a Hebel-Schlicter peak, and the data is consistent with d-wave superconductivity. These experiments give evidence for d-wave superconductivity twice: the lack of a Hebel-Schlicter peak and the large σ_1 due to quasiparticle effects. Note that the other sharp peak right at T_c is believed to be due to fluctuations of superconductivity. Its functional form is also inconsistent with it being a Hebel-Schlicter peak.

Spin density wave compounds which can be treated within the BCS formalism are also expected to have a type I order parameter and a gap edge enhancement.

A vast literature exists on the electrodynamics of superconductors. I have given only the most superficial treatment here. Many considerations go into how superconductivity is exhibited in optical spectra. See Tinkham (57) or Dressel and Grüner (8), for instance, for in-depth discussions on the clean and dirty limits of superconductivity and Basov and Timusk (34) for the state-of-the-art on high-temperature superconductivity.

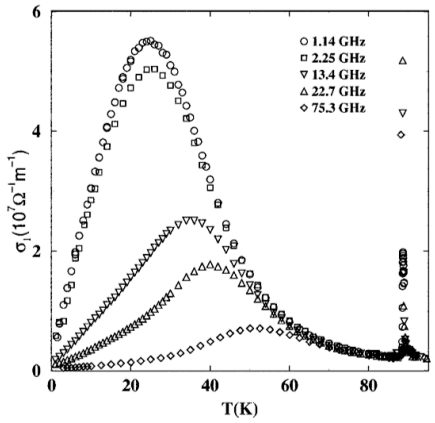

FIG. 31 The real part of the conductivity extracted from the microwave surface resistance of YBCO at a number of different GHz frequencies. From (61).

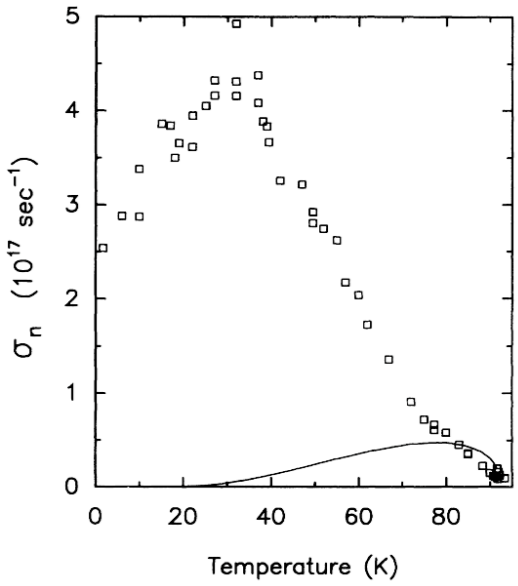

FIG. 32 The real part of the conductivity extracted from the microwave surface resistance of YBCO at a number of different GHz frequencies (squares). The BCS conductivity (solid) is calculated using a T_c of 91.8 K, a gap ratio of 3.52, and various other physical parameters such as penetration depth, coherence length, and mean free path. From Ref. (62).

V. ADVANCED ANALYSIS

A. Sum Rules

The optical constants satisfy a number of different sum rules (10). The most frequently used sum over the real conductivity is the one that will be discussed here. As alluded to above, there is a relation for the integral over all frequencies of the real part of the conductivity to the total number of charges and their mass.

$$8\int_0^\infty \sigma_1(\omega)d\omega = \frac{4\pi n e^2}{m_e}. \tag{50}$$

Analysis of data in terms of sum rules provides a powerful tool that can be used to study spectral weight distributions in a relatively model free fashion. The above integral which extends from zero to infinity is the *global oscillator strength sum rule*, which relates the integral of the σ_1 to the density of particles and their bare mass. This analysis applied to the simple metal case of aluminum is shown in Fig. 33. Aluminum's nominal electronic configuration is $1s^2$, $2s^2$, $2p^6$, $3s^2$, $3p^1$. Depending on the cutoff of the integral, the sum rule for different orbitals is satisfied. Integrating up the approximately the plasma frequency (15.5 eV) returns the number of electrons in the $n = 3$ valence band. At the x-ray L edge at around 100 eV, one begins to reveal spectral weight of the $n = 2$ formed bands. One can see that if the integral is performed to high enough energies (well above the K edge of aluminum) one recovers the aluminum's atomic number '13'.

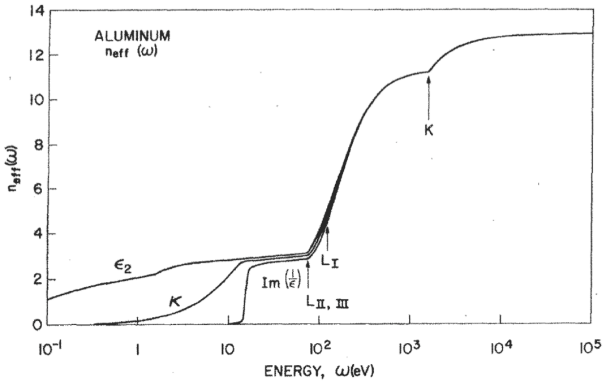

FIG. 33 The effective number of carriers $n_{eff}(\Omega_c)$ as a function of cutoff frequency Ω_c for Aluminum. A number of different sum rules are investigated and displayed. The sum rule for ϵ_1 is equivalent to the sum rule expressed in Eq. 50. Figure adapted from Ref. (63).

The integral to infinite frequencies is rarely utilized in practice and we are usually more concerned with partial sum rules such as

$$8\int_0^W \sigma_1(\omega)d\omega = \frac{4\pi n e^2}{m_b}. \tag{51}$$

where W is the unrenormalized electronic bandwidth and m_b is the band mass. In correlated systems one frequently makes use of an even more limited sum rule and only performs the integral over an energy several times the Drude width to determine the mass renormalized due to interactions. The small spectral weight in a very narrow Drude peak as shown in Fig. 8 gives a very large

mass. An integral as such over a renormalized Drude peak with small spectral weight is how the very large masses in Fig. 4 were generated.

Sum rules have been used extensively in the analysis of the data for correlated electron systems because, in some circumstances, they allow a relatively model independent way to analyze the data. For instance, one can show that for a tight binding model with nearest neighbor interactions that

$$8\int_0^W \sigma_1(\omega)d\omega = -\frac{\pi e^2 a_r}{2\hbar^2}K_r. \tag{52}$$

where a_r is the lattice constance in the incident E field's polarization direction and K_r is the effective kinetic energy. This relation has been used extensively in the cuprate superconductors to attempt to show evidence for a novel lowering of the kinetic energy-driven mechanism for superconductivity. This is in contrast to the usual mechanism in the BCS theory where it is the potential energy that drops when falling into the superconducting state. Such analysis is not trivial in these materials, as there is evidence that the spectral weight that goes into the condensate is derived not just from the near E_F electronic band over a width much smaller than W, but over an energy range many times the band width W.

For instance, it is believed that the usual sum rule for superconductors (Ferrell-Glover-Tinkham) is satisfied for the *ab* plane conductivity of the cuprate superconductors up to about 10% accuracy (34). Using spectroscopic ellipsometry, Molegraaf *et al.* (64) used a combination of reflectivity and spectroscopic ellipsometry in Bi2212 to conclude that about 0.2 - 0.3% of the total strength of the superconducting δ funtion is collected from an energy range beyond 10,000 cm^{-1} to 20,000 cm^{-1} (Fig. 34) and that the kinetic energy does decrease in the superconducting state. This is a very small effect, but still large enough to account for the condensation energy. Such analysis of total spectral weight transfer can be tricky as it requires the analysis of spectral weight beyond the measurement regime. These results or rather the analysis of the data has been disputed by Boris *et al.*, (65) who form a nearly opposite conclusion regarding spectral weight transfer based on nearly identical experimental data.

The c-axis response has been investigated in a similar manner and a similar transfer of spectral weight from very high energies to the δ function has been observed, although in this case the magnitude of the effect is definitively insufficient to account for T_c (34).

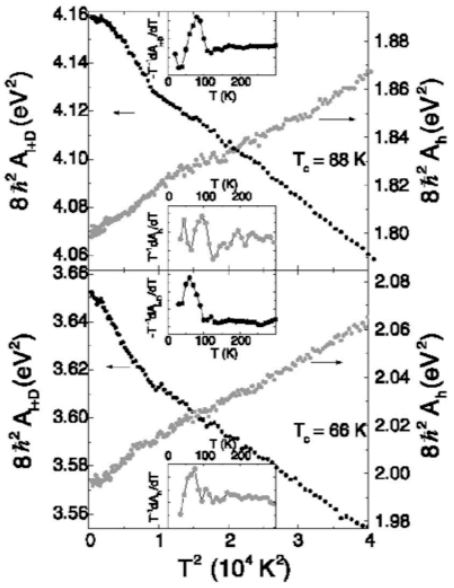

FIG. 34 Temperature dependence of the low-frequency spectral weight $A_{1+D}(T)$ and the high-frequency spectral weight $A_h(T)$, for optimally doped and underdoped Bi2212. Insets: derivatives $-T^{-1}dA_{1+D}/dT$ and $T^{-1}dA_{1h}/dT$. From Ref. (64).

B. Extended Drude Model

Within the Drude-Lorentz (Sec. II.B) model we consider that conduction electrons are quasi-free. The relaxation rate of the Drude intraband contribution is considered to be characterized by a single frequency independent relaxation time τ. It is well known however that various channels can contribute to relaxation in solids, each with a characteristic frequency dependence. For instance, in 3D the charge-charge scattering rate is expected to exhibit an ω^2 dependence at low frequency. An electron scattering off an Einstein boson (a single spectral mode with a well-define frequency ω_0) is expected to show an onset in scattering at the boson frequency ω_0.

Allen and Mikkelsen (66) proposed that one could capture these frequency dependences in optical spectra through an *extended Drude model* (EDM) where the mass and scattering rate are explicitly frequency dependent. Inverting the complex conductivity one gets

$$\frac{m^*(\omega)}{m_b} = -\frac{\omega_p^2}{4\pi\omega}Im\left[\frac{1}{\sigma(\omega)}\right], \tag{53}$$

$$\frac{1}{\tau(\omega)} = \frac{\omega_p^2}{4\pi}Re\left[\frac{1}{\sigma(\omega)}\right]. \tag{54}$$

where m_b is the band mass.

Both in spirit and formalism this is equivalent to standard treatments in many-body physics where one posits that the effects of interactions can be captured by shifting the energy of an electron added to an interacting ensemble from the bare non-interacting energy $\epsilon(\mathbf{k})$ by a complex *self-energy* $\Sigma(\omega,\mathbf{k}) = \Sigma_1(\omega,\mathbf{k}) + i\Sigma_2(\omega,\mathbf{k})$.

One can express the optical response in terms of the complex self-energy $\Sigma^{op}(\omega) = \Sigma_1^{op}(\omega) + i\Sigma_2^{op}(\omega)$ as

$$\sigma(\omega) = -i\frac{\omega_p^2}{4\pi(2\Sigma^{op}(\omega) - \omega)}. \quad (55)$$

and in terms of previously defined quantities

$$\Sigma_1^{op} = \frac{\omega}{2}(1 - m^*/m_b),$$
$$\Sigma_2^{op} = -\frac{1}{2\tau(\omega)}. \quad (56)$$

A caveat should be given about the interpretation of optical self-energies. Although an identification can be made with the quasi-particle self-energies found in one particle spectral functions, the two self-energies are not exactly the same. While quasi-particle scattering depends only on the total charge scattering rate to all final states, backward scattering gives a much bigger contribution to lifetime effects than forward scattering in transport and optics, because it degrades the momentum much more efficiently. In general this means that the quantities derived *via* optics emphasize backward scattering over forward scattering and so the optically derived quantities can contain a vertex correction not included in the full quasi-particle interaction. In this sense the two self-energies are different although they contain much of the same information.

Frequently the extended Drude model will be introduced in terms of a complex frequency dependent *Memory* function, $M(\omega) = 1/\tau(\omega) - i\omega\lambda(\omega)$, where τ is the lifetime and $1 + \lambda = m^*/m_b$

$$\sigma(\omega) = \frac{\omega_p^2}{4\pi(M(\omega) - i\omega)}, \quad (57)$$

$$\sigma(\omega) = \frac{\omega_p^2}{4\pi(1/\tau(\omega) - i\omega[1 + \lambda(\omega)])}. \quad (58)$$

One can put Eq. 58 in the form of the standard Drude model with the substitutions $\tau^*(\omega) = [1 + \lambda(\omega)]\tau(\omega)$ and $\omega_p^{*2} = [1 + \lambda(\omega)]\omega_p^2$ to get

$$\sigma(\omega) = \frac{\omega_p^{*2}(\omega)}{4\pi(1/\tau^*(\omega) - i\omega)}. \quad (59)$$

This equation describes the frequency dependence of a particle with renormalized plasma frequency (and hence renormalized mass) and renormalized scattering rate. Note that the quantity $1/\tau^*$ is not equivalent to the quantity defined in Eq. 54 above, as $1/\tau^*$ includes the renormalization effects of the lifetime as well as the mass, whereas $1/\tau$ includes only lifetime effects. The two quantities differ by a factor of $1+\lambda(\omega)$. In this sense $1/\tau(\omega)$ is the more intrinsic quantity, as also evidence by its direct proportionality to the imaginary part of the self-energy. For weak frequency dependence $1/\tau^*$ is the actual half width of the Drude peak in the optical conductivity.

Various contributions to the total scattering rate such as electron-electron (ee), electron-phonon (ep), electron magnon (em), etc. add within the prescription set by Matthiesen's rule as $\frac{1}{\tau(\omega)} = \frac{1}{\tau_0} + \frac{1}{\tau_{ee}} + \frac{1}{\tau_{ep}} + \frac{1}{\tau_{em}}$. Note that there is also typically a contribution $\frac{1}{\tau_0}$ to the elastic scattering which is frequency independent that comes from static disorder. As mentioned above this can be seen as a measure of the degree to which the translational symmetry is broken by disorder and hence the degree to which strict momentum conservation in the optical selection rule $\mathbf{q} = 0$ can be violated.

As $\frac{1}{\tau(\omega)}$ and $m^*(\omega)$ are a particular parameterization of the real and imaginary parts of a complex response function, they are Kramers-Kronig related. Analogous to the case of $\sigma(\omega)$ detailed above, if one knows $\frac{1}{\tau(\omega)}$ for all ω, then $m^*(\omega)$ can be calculated and vice versa.

The near-E_F electrons of the noble metals, like Cu, Ag, and Au are free-electron-like s-states, which form a Fermi surface that deviates from almost spherical symmetry only near the Brillouin zone necks in the $< 111 >$ directions. The above analysis applied to such metals is shown in Fig. 35 and Fig. 36. The scattering rate shows an almost ideal ω^2 dependence of the scattering rate, which is in accord with the expectation for electron-electron scattering. It is interesting that electron-electron scattering is observed up to such high energies as we may have expected other contributions such as electron-phonon scattering also to give an observable contribution. We should reiterate that a purely translational invariant electron gas, cannot dissipate momentum by electron-electron collisions alone. In this regard effects like umklapp scattering are essential to see the effects of such collisions in the optical response.

Note that in Eqs. 53 and 54 there is the matter of how to define the plasma frequency ω_p. For the electron gas the plasma frequency is given by $4\pi ne^2/m$, however the precise definition is less clear in a real material with interactions and interband transitions. In the above analysis ω_p must come from the spectral weight of the full intraband contribution. Rigourously the plasma frequency should be defined from the sum rule as

$$\int_0^\infty \sigma_1^{intra}(\omega) = \frac{\omega_p^2}{8}. \quad (60)$$

where σ_1^{intra} is contribution to the conductivity coming from all *intraband* spectral weight. The integral extends all the way to infinity, which gives of course a practical difficulty in real systems because the value of the spectral weight will be contaminated by *interband* contributions. Note that for a complicated interacting system the integral and ω_p must include not only the contributions of the weight of the low frequency Drude peak, but must also include higher energy parts of the spectra if their origin is from the same intraband excitations. It can be difficult experimentally to estimate ω_p accurately. For instance, in the case of a system with strong electron-phonon coupling the spectra may be approximately modeled as the

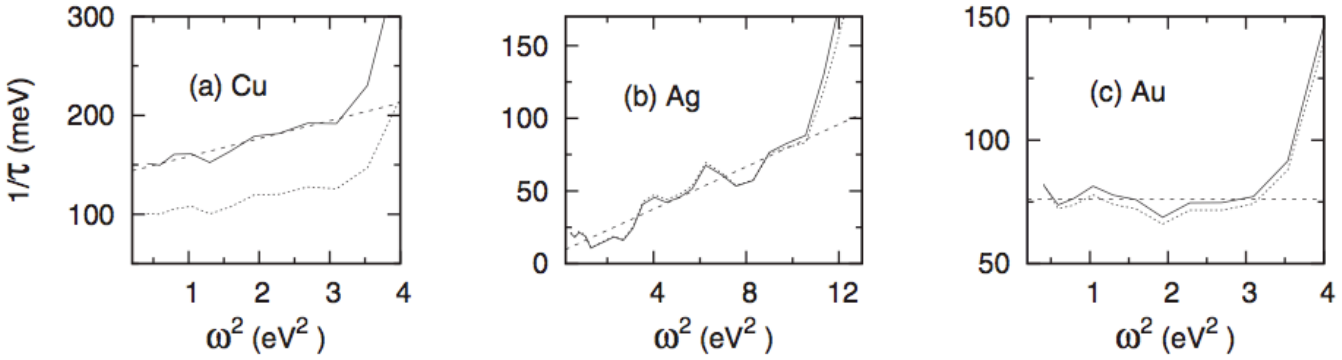

FIG. 35 Scattering rate vs. ω^2 of (a) Cu, (b) Ag and (c) Au. Solid and dotted lines are the bare scattering rate $1/\tau_0$ and the dressed scattering rate $1/\tau$ respectively as detailed in the text. From (67)

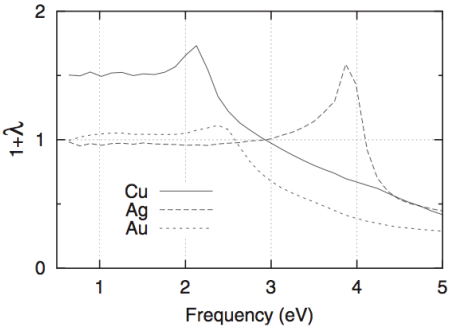

FIG. 36 Mass enhancement factor $1+\lambda$ of noble metals. From (67)

usual Drude model with a simple $\omega = 0$ Lorenztian and frequency independent scattering rate at low frequencies, but with a higher frequency satellite at the characteristic phonon frequency which results physically from the excitation of a *real* phonon as well as an electron-hole pair. The high frequency satellite manifests in the scattering rate as an onset at the phonon frequency as an additional decay channel becomes available at that energy. In this sense the plasma frequency which goes into an extended Drude analysis is the plasma frequency associated with the spectral weight of both the low frequency 'Drude' contribution *and* the satellite. The spectral weight of the low frequency part may be clear, but it may be a difficult practical matter to clearly identify the spectral weight of the satellite, due to the overlapping contributions of it with true interband transitions etc. In practice, a high frequency cutoff to the integral in Eq. 60 is usually set at some value which is believed to capture most of the intraband contribution, while minimizing contamination by interband transitions. A number of different criteria can be used: the requirement that the intergral is temperature independent, an appeal to reliable band structure calculations etc.

There can also be a difficulty in definitions of the plasma frequency for systems described by, for instance, the Mott-Hubbard model, where a strong onsite repulsion splits a single metallic band into upper and lower Hubbard 'bands'. In such cases, one has one band or two depending on definitions and so the matter of the true intraband spectral weight can also be poorly defined. In such cases it is important to remember that in this and other cases that the Drude model is a classical model applicable only to weakly interacting mobile particles. Although the EDM can be put on more rigorous ground expressing its quantities as optical self-energies, one still always makes analogy and connection to a non-interacting system. To the extent that the EDM is just a parameterization of optical spectral, it is always valid. However, to the extent that its output can be interpreted as a real mass and scattering rate of *something*, it is important that that something exists. In other words, it must be valid to discuss the existence of well-defined electronic excitations in the Fermi-liquid sense in the energy regimes of interest.

The EDM has been used in many different contexts in strongly correlated systems. An ideal example is afforded by its application to heavy fermion systems. As mentioned above, due to interaction of conduction electrons with localized moments the conduction electrons can undergo extremely large mass renormalizations of a factor of a few hundred over the free electron mass. These mass renormalizations develop below a coherence temperature T^*. Such effects are reflected in the optical spectra. As seen in Fig. 37, at high temperatures an EDM analysis reveals a pure Drude-like essentially frequency independent mass and scattering rate. The small mass and large scattering rate at high temperatures reflect the effects of essentially normal electron scattering strongly and incoherently with the localized moments. The spectra show no particularly interesting frequency dependence. Below the coherence temperature at low frequencies significant renormalizations to the mass and scattering rate are seen. The mass develops a significant enhancement and the scattering rate drops. The coher-

ence temperature T^* and the frequency above which the unrenormalized values are recovered ω_c are equivalent to each other to within factors of order unity. Remarkably the optical mass as compared to the band mass is increased by a factor of almost 350. Note that although both the mass and the low frequency scattering rate undergo dramatic changes, the DC Drude conductivity is not changed signifiantly, as $\sigma_{DC} \propto \tau/m$ and the respective changes approximately cancel. This is reflected in the fact that the relation $m^*(\omega \to 0)/m_b$ is expected to be equivalent to $\tau/\tau^*(\omega \to 0)$ to within factors of order unity (68). Note that these changes in scattering rate and mass are reflected in the optical conductivity itself by the formation of a very sharp zero frequency mode (essentially a Drude peak) which rides on top of the normal Drude peak (68).

Evidence that the renormalizations in the optical mass reflect the existence of real heavy particles in these systems and not just a convenient parametrization of the optical spectral can be seen in the above discussed Fig. 4 which shows a proportionality of the optically measured mass to the linear coefficient of the specific heat (which is proportional to inverse of the near E_F density of states). It is remarkable that a parameter determined dynamically - essentially by shaking charge with an oscillating E-field - is precisely related to a quantity which is determined *thermodynamically* by quantifyng the amount of heat absorbed. This graph provides a remarkable demonstration of the quasiparticle concept!

In addition to electron-electron scattering, the effects of electron-boson interactions also reveal themselves in the optical spectra. Spectral features in the optical conductivity deriving from electron-boson coupling were orginally discussed in the context of Holstein processes - the creation of a real phonon and an electron-hole pair with the absorption of a photon - in superconducting Pb films (69; 70). As mentioned above, the EDM analysis can reveal significant information about the interaction of electrons with various bosonic modes.

In Fig. 38 the optical conductivity calculated for an electron with impurity scattering coupled to a single Einstein phonon is shown for a few temperatures. (See Puchkov, Allen, Shulga (72) for details regarding the calculation of the effects of electron-boson scattering in optical spectral.) The lower two panels show the scattering rate and mass enhancement generated from the optical conductivity. At low temperatures the optical conductivity (Fig. 38 (top)) reveals a sharp Drude peak at low frequencies, which results from the usual electron-hole excitations. The sharp onset in absorption at the phonon frequency is the threshold for excitation of a *real* phonon. At threshold, electron-hole pairs are excited additionally, but it is the phonon which carries away most of the energy. This is reflected in the scattering rate, which is flat and small at low ω, but shows a cusp and sudden increase at ω_0 as the phase space for scattering increases discontiously (Fig. 38 (middle)).

Although real phonons can only be excited above

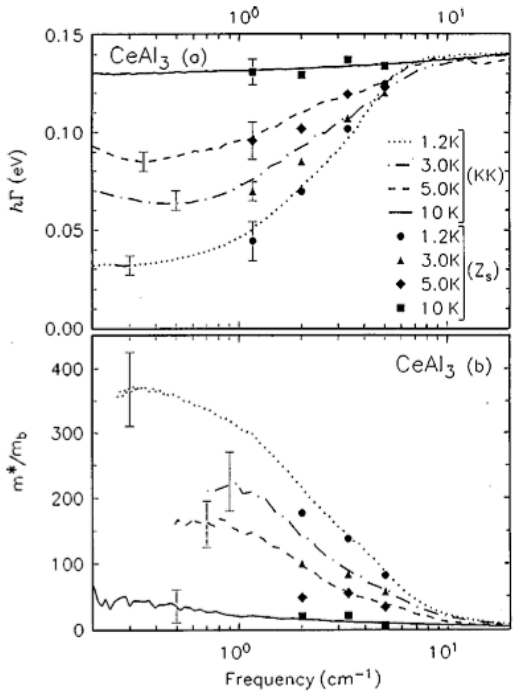

FIG. 37 Scattering rate and effective mass in $CeAl_3$. (a) Frequency-dependent optical scattering rate for $CeAl_3$ at four temperatures, compiled using both infrared reflectivity and microwave cavity data. (b) Frequency dependence of m^* obtained from Eq. 54 (71).

threshold, electron-phonon coupling manifests itself at energies below threshold by an increase in the effective mass (Fig. 38 (bottom)). Physically, this can be understood as a renormalization of the electron-hole pair energy, which is modified by the excitation of *virtual* phonons. This renormalization of the energy manifests itself as an increased mass. The electron-hole pair can be viewed as being surrounded by a cloud of virtual phonons.

One can get an approximate measure of the boson coupling function as (73)

$$\alpha^2 F(\omega) = \frac{1}{2\pi}\frac{d^2}{d\omega^2}[\omega Re\frac{1}{\sigma(\omega)}]. \qquad (61)$$

Although the results of the calculation diplayed in Fig. 38 is for phonons, the general idea holds generically for electron-boson coupling (73; 74) although, of course, the bosonic density of states is generally more complicated than a single sharp mode. Recently Tediosi *et al.* (75) found a remarkable example of this general idea in semimetal bismuth, where the bosonic excitation is formed out of the collective excitations of the electronic ensemble itself i.e. the plasmon. This is an effect that should be present in all metals, but is enhanced in a semi-metal like bismuth due to its very low carrier density and high $\epsilon_\infty \approx 100$. At low frequencies Tediosi *et al.* (75) found

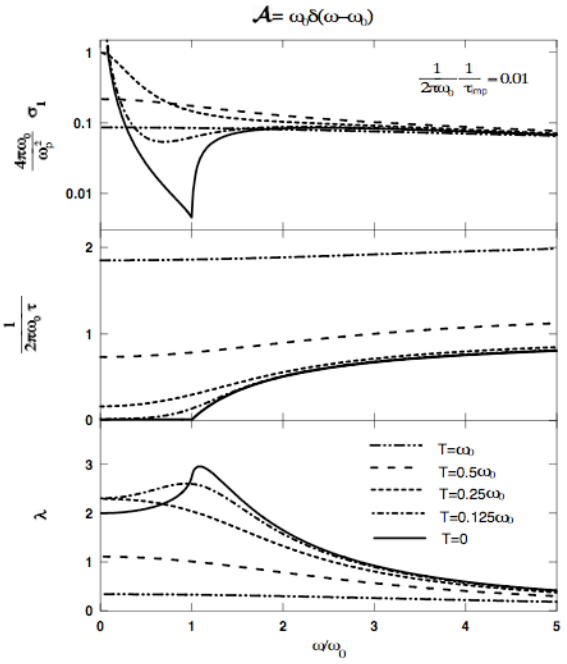

FIG. 38 Electron-boson model calculations with a boson spectral density $A(\Omega) = \omega_0\delta(\omega - \omega_0)$. The top panel gives the optical conductivity and the lower two panels show the corresponding scattering rate and mass enhancement. The coupling constant in this calculation is set to 1. From (72).

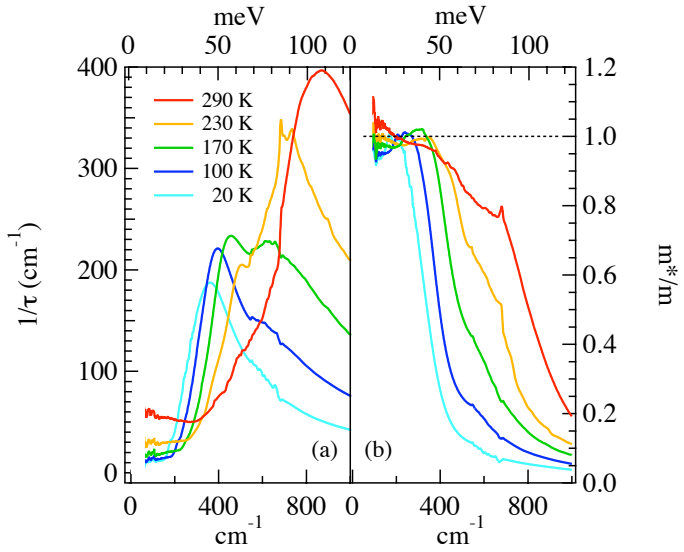

FIG. 39 (Color) Frequency dependent scattering rate (a) and effective mass (b), calculated from the optical data of elemental bismuth using ϵ_∞. The low frequency scattering rate $\tau^{-1}(\omega)$ progressivly falls as the temperature is lowered. An approximately frequency independent region is interrupted by a sharp onset in scattering and a decrease of the effective mass.

in their EDM analysis (Fig. 39) that the mass and scattering rate are approximately frequency independent as expected for the Drude model. However, at higher frequencies there is sharp onset in the scattering rate at a strongly temerpature dependent position. As one cools bismuth, the charge density changes dramatically and the plasmon frequency (as given by the zero crossing of ϵ_1) drops by a factor of almost two. It was found that the energy scale of this sharp onset in scattering tracks this independently measured plasmon frequency as shown in Fig. 40. One can note the strong resemblance of the data to the calculation of an electron interacting with sharp mode in Fig. 38. A strong coupling as such between electrons and plasmonic electron degrees of freedom may in fact be captured within the same Holstein Hamiltonian that is used to treat the electron - longitudinal phonon coupling and describe polarons. As a result, this collective composite excitation has been called a *plasmaron* (76; 77) when exhibited in the single particle spectral function. The observation of Tediosi *et al.* was the first such observation optically.

EDM analysis has been applied extensively to the high-T_c cuprate superconductors (34). In Fig. 41 I show the imaginary and real parts of the optical self-energy as defined in Eq. 56 above for a series of four doping levels of the compound $Bi_2Sr_2CaCu_2O_{8+\delta}$ (78). The displayed samples span the doping range from the underdoped to the severely overdoped. Again one can notice the resem-

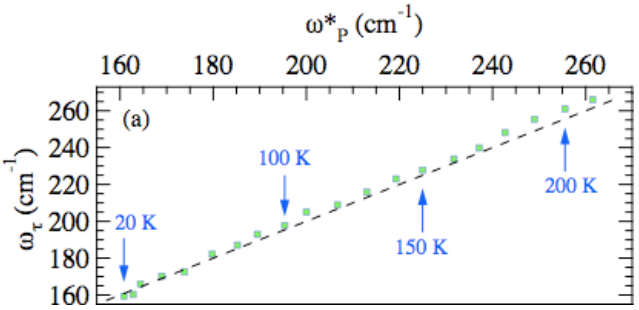

FIG. 40 A parametric plot of the sharp onset in scattering plotted versus the independently measured plasmon frequency in elemental bismuth. The plasmon frequency changes monotonically as the sample is cooled from room temperature to 15K.

blance of the data to that of the model calculation in Fig. 38 and indeed data of this kind, along with similar signatures in angle-resolved photoemission have been interpreted as generic signatures of electron-boson interaction in the cuprates.

The identity of this boson is a matter of intense debate in the community with some groups favoring interaction with magnetism and notably the famous '41 meV' resonance mode and other groups claiming that interaction

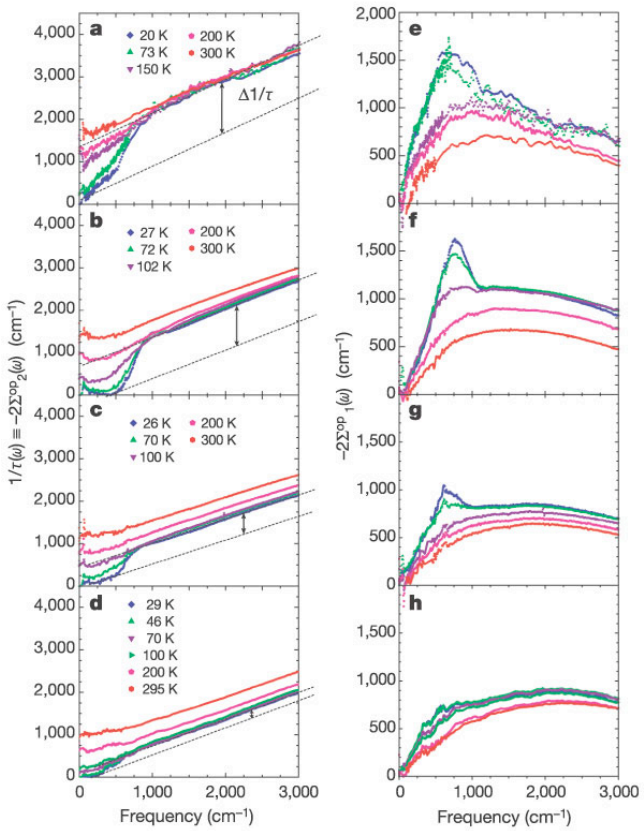

FIG. 41 (Color) a-d, The frequency and temperature dependent optical scattering rate, $1/\tau(\omega)$ for four doping levels of $Bi_2Sr_2CaCu_2O_{8+\delta}$. a, $T_c = 67$ K (underdoped); b, 96 K (optimal); c, 82 K (overdoped); d, 60 K (overdoped). eh, The real part of the optical self-energy, - $2\Sigma_1^{op}(\omega)$ as defined in Eq. 56

with phonons more accurately describes the data.[1]

C. Frequency dependent scaling near quantum critical points.

A quantum phase transition (QPT) is a zero-temperature transition between two distinct ground states as a function of a non-thermal parameter, such as magnetic field, pressure, charge density etc. (79; 80). Unlike conventional phase transitions, which are driven by thermal fluctuations they are driven essentially by diverging fluctuations of the system's zero point motion. Once thought to be only of academic interest, the existence of a QPT nearby in a material's parameter space is believed to influence a whole host of finite temperature properties. QPTs may hold the key to understanding the unusual behavior of many systems at the forefront of condensed matter physics (79).

Just as in the case of conventional phase transitions, QPTs are believed to be characterized by diverging length and time scales if second order. In the disordered state, one envisions an order parameter that fluctuates slower and slower over longer and longer length scales until at the transition these length and time scales diverge. These length and time scales are the correlation length ξ_c and time τ_c. The divergence of the fluctuation time scales, which in the case of conventional transitions is called *critical slowing down* implies the existence of a characteristic frequency ω_c which vanishes at the transition.

In a QPT, the transition occurs as a function of some non-thermal parameter K. It is usually considered that close to the transition at K_c, ξ_c diverges in a manner $\propto |K - K_c|^{-\nu}$ and τ_c diverges $\propto |K - K_c|^{-z\nu} \sim \xi^z$ where ν and z are called the correlation length and dynamic exponent respectively.

From the classical case, a well established formalism exists for the understanding of various physical quantities close to continuous (2nd order) transitions. Widom's scaling hypothesis assumes that close to the transition the *only* relevant length and time scales are those associated with diverging correlations in the order parameter (81). Such considerations hold for QPTs also and mean that physical observables such as magnetization or conductivity are expected to have scaling forms, in which independent variables such as the temperature, probe frequency or wave vector appear in the argument only as a product with quantities like ξ_c and τ_c. This is expressed formally in terms of $finite-size$ scaling. For an incident wave vector $q = 0$ such a scaling form can be written

$$O(K, \omega, T) = \frac{1}{T^{d_o/z}} F(\omega/T, T\tau_c). \qquad (62)$$

Here O is some observable and F is the scaling function. d_o is the scaling dimension, which determines how various physical quantities change under a renormalization group transformation. It is often close to the "engineering" dimension of the system (for instance 0 for 2D conductivity), but can acquire an anomalous dimension in certain circumstances. For further discussion on scaling forms and motivation on this and other related points see the excellent review by Sondhi *et al.* (79).

Scaling functions written as a function of ξ_c and τ_c can be very powerful as they allow the analysis of experimental data independent of microscopic theory. For instance, the scaling exponents ν and z only depend on

[1] My (NPA's) opinion is these are by and large straw-man arguments and perhaps not really the right way to approach the problem. In a strongly correlated system like high-T_c superconductors, it is clear that everything is strongly coupled to everything else and magnetism is strongly connected to lattice effects and vice versa. In this regard, it is not surprising that experiments sensitive to the lattice show lattice effects and experiments sensitive to magnetism show magnetic effects. One should not expect in such materials that various degrees of freedom neatly partition in separate distinct subsystems.

certain global properties of the system such as symmetry, dimensionality, and the nature of the dominant interactions.

There are many studies where the existence of a QPT is inferred from frequency dependent scaling (see for example (82)), but there are far fewer studies where scaling is investigated as one passes through a known QPT. I know of only two where scaling in the frequency dependent conductivity has been investigated. This is unfortunate because, as mentioned, such studies could potentially be tremendously powerful for the investigation of correlated systems where the underlying physical model is not clear. This shows the extreme experimental challenges inherent in accessing the experimentally relevant frequency and temperature ranges where $\hbar\omega \gg k_B T$ while both $\hbar\omega$ and $k_B T$ are as low as possible, but also below any higher energy scales that are not relevant to the ordered state. Hopefully this situation will change with the increasing prominence and usability of broadband microwave and THz techniques.

The first experimental study to investigate frequency dependent scaling near a QPT was that of Engel *et al.* (83), who used a waveguide coplanar transmission setup to perform broadband microwave range spectroscopy on quantum Hall systems. In quantum Hall systems the longitudinal resistivity goes to zero at field values where the transverse resistivity assumes perfectly quantized values. Although the value of the Hall resistivity is perfectly quantized, the width of the transition region depends on temperature (84) and on measurement frequency (83). In Fig. 42 the Re σ_{xx} vs. B is shown at three different frequencies and two different temperatures. One can see that at 50 mK, the width of the transitions regions is strongly frequency dependent, while at 470 mK the widths are almost frequency independent.

This frequency and temperature dependence of ΔB (as defined as the extrema of the derivatives of Re σ_{xx}) is summarized in Fig. 43 for one of the spin-split levels. Similar data is found for other levels. One sees that for all such levels at low frequencies, the data are frequency independent, whereas for low temperatures the data are temperature independent. The crossover between regimes takes place when $3\hbar\omega \sim k_B T$. Such data is consistent with scaling theories of quantum criticality, where the only relevant frequency scale at the QPT is set by the temperature itself. It is also significant that the crossover condition involves $\hbar$, showing that the physics is essentially quantum mechanical. In the high frequency data it is observed that spin split levels give a ΔB which is approximately $\propto \omega^{\gamma}$, with $\gamma = 0.43$. This is consistent with scaling theories that give the exponent for quantum percolation of $1/\gamma = z\nu = 7/3$ and also consistent with the temperature dependence of these transition widths as measured by DC transport that show a $T^{\frac{1}{7/3}}$ dependence. It was claimed that through an analysis of both the temperature and frequency dependent exponents, one can extract the dynamic exponent z, which yields $z = 1$. This is consistent with long range Coulomb interaction.

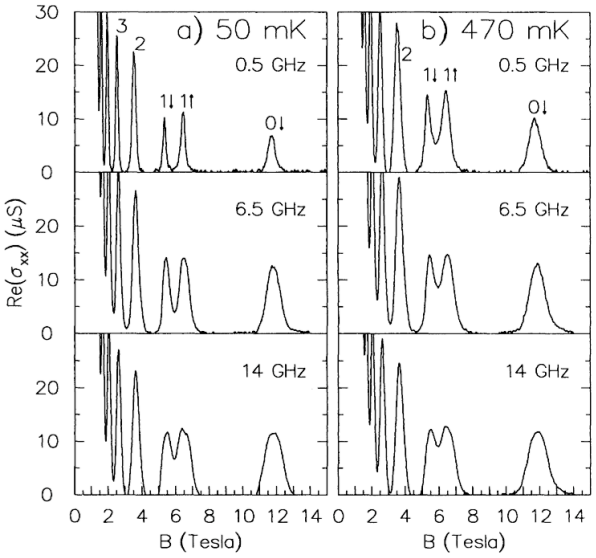

FIG. 42 (Color) Re σ_{xx} vs. B at three frequencies and two temperatures. Peaks are marked with Landau level N and spin index.

Both the DC data (84) and the high frequency data have transition widths which exhibit a power law dependence on temperature or frequency with an exponent of 3/7 at all spin-split transitions, showing that all such transitions between quantum Hall levels fall into the same universality class. It should be possible in such a study to incorporate both temperature and frequency dependence into a single scaling function although this has not been done yet. It is expected that a general scaling function of the form

$$\rho(B, T, \omega) = F(\omega/T, \delta/T^{\frac{1}{z\nu}}). \tag{63}$$

applies where $\delta = |B - B_c|/B_c$ measures the distance to the quantum critical point. This function is equivalent to Eq. 62 using the fact that the scaling dimension of the resistivity vanishes in $d = 2$. In the high frequency and high temperature limits, Eq. 64 reduces to one where frequency and temperature appear in the arguments as $\frac{\delta}{\omega^{1/z\nu}}$ and $\frac{\delta}{T^{1/z\nu}}$.

Lee *et al.* (85; 86) applied the ideas of finite size scaling to the 3D metal-insulator (MI) transition in $Nb_{1-x}Si_x$. They measured the frequency dependent conductivity *via* millimeter wave transmission through thin films whose relative concentrations of Nb to Si were tuned to exactly to the MI QPT point at x_c. As in the study of Engel *et al.* (83), for samples tuned right to quantum criticality it is observed that for the $\hbar\omega >> k_B T$ data the conductivity is temperature independent and that for $\hbar\omega \ll k_B T$, the data are frequency independent (Fig. 44). A crossover from a frequency dominated regime to a temperature dominated regime implies the existence of a scaling function $\sum$ of a form that can be inferred from above Eq. 62

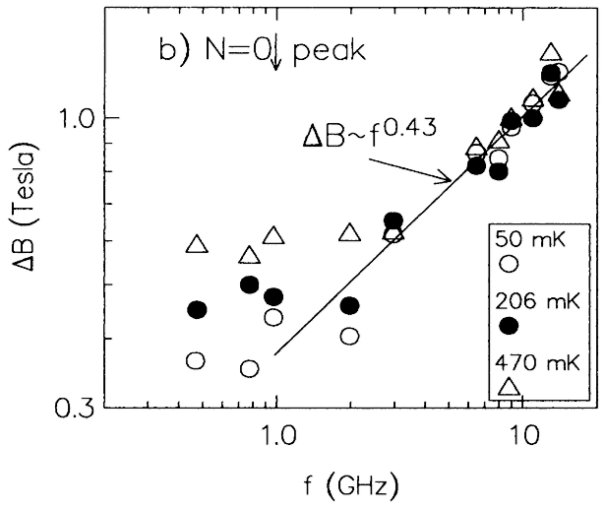

FIG. 43 (Color) Peak width between extremal points in longitudinal resistance d Re σ_{xx}/dB ΔB vs. measurement frequency at three different temperatures. Data is shown for the $N = 0 \downarrow$ Landau level.

$$\sigma(x_c, T, \omega) = CT^{\frac{1}{z}} \sum (\frac{\hbar\omega}{k_B T}). \tag{64}$$

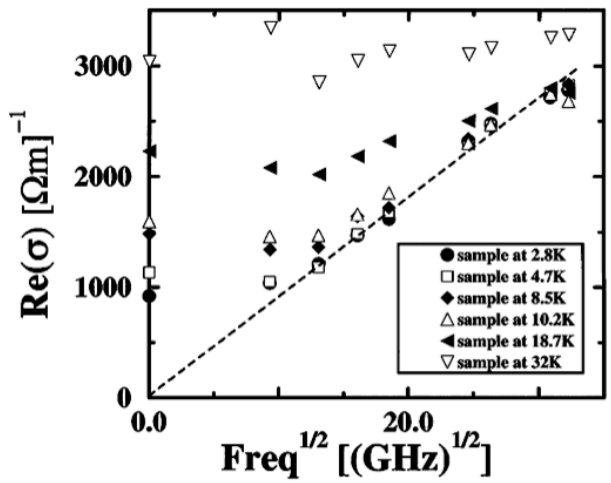

FIG. 44 Re$\sigma(\omega)$ plotted against $\sqrt{\omega}$ for temperatures 2.8 to 32K and frequencies 87-1040 GHz. For the lowest temperatures and when $\hbar\omega > k_B T$, the data follow a $\sqrt{\omega}$. The data approaches the DC values plotted on the vertical axis for $\hbar\omega \ll k_B T$.

In previous work on similar samples it was found that for samples tuned to the critical concentration the DC conductivity followed a $T^{1/2}$ relation implying $z = 2$. As shown in Fig. 45, successful scaling can be found by plotting the scaled conductivity Re $\sigma(T, \omega)/CT^{1/z}$ using this z. This procedure collapses the data over the entire measured frequency range for temperatures 16 K and below, implying the applicability of a scaling function that depends *only* on the scaled frequency. Data for temperatures higher than 16 K starts to rise above the other collapsed curves, indicating the appearance of other mechanisms (electron-phonon scattering for example) which limits the size of quantum fluctuations. This is consistent with the DC result where the conductivity starts to deviate from the $T^{\frac{1}{2}}$ above 16 K.

As already inferred from Fig. 44, the scaling function shows both temperature and frequency dominated regimes, with a crossover at approximately $\hbar\omega \sim k_B T$. Again, this shows that at the QPT the only energy scale is set by the temperature itself. Note, that this crossover happens at a slightly different ω/T ratio than the quantum Hall case, but is still of order unity as expected. For high frequencies the scaling function follows a power law dependence with the same exponent as was used to scale the vertical axis with $z = 2$. This means that an equivalent scaling function could have been found by dividing the conductivity data by $\omega^{\frac{1}{2}}$ and plotting the data as a function of T/ω. Lee *et al.* (85) attempted to guess the form of the scaling function with the expression $\sum = Re(1 - ib\hbar\omega/k_B T)^{1/2})$. The function successfully captures the high and low ω/T, but misses the sharp crossover near $\hbar\omega/k_B T \sim 1$.

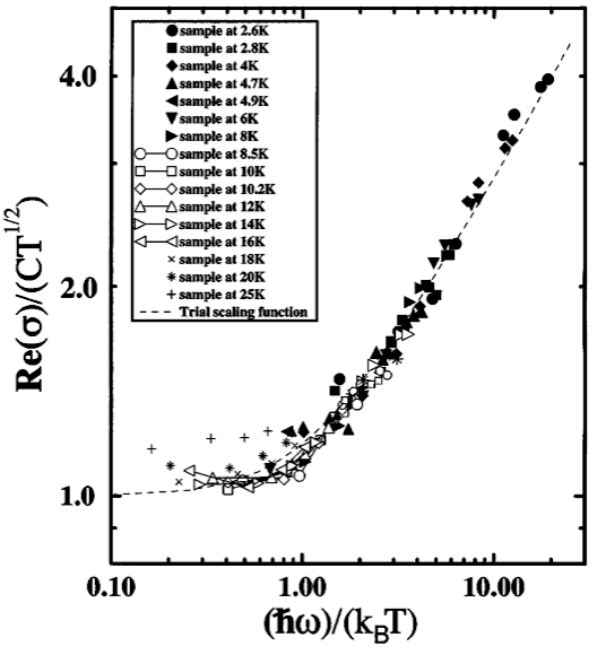

FIG. 45 Log-log plot of conductivity scaled by the factor $C = 475(\Omega m K^{1/2})^{-1}$ vs. ω/T. For temperatures 16 K and below, the data for the entire experimental frequency range collapse onto a single curve within the experimental noise. Higher temperature data begins to rise above the collapsed data systematically for low scaled frequencies. The dashed line is a trial scaling function as described in the text.

The value of the dynamic exponent $z = 2$ is interesting.

It is different than what is expected from models without a density of states singularity, where $z = d$ or for those with straight Coulomb interation ($z = 1$ observed in the quantum Hall case). It is consistent with several field-theoretic scenarios which give $z = 2$ (87).

I should mention that as presented above, frequency scaling does not necessarily give us any information on exponents etc. that we could not also get from the temperature scaling. Here the primary importance of frequency scaling was in its ability to demonstrate how characteristic time scales diverge at the QPT and leave the temperature itself as the only energy scale in the problem. However, as discussed by Damle and Sachdev (88), the fact that at the QPT itself, response functions can written as a universal function of ω/T, one does not necessarily expect the same behavior in the $\omega = 0$, $T \to 0$ (incoherent) limit as in the $\omega \to 0$, $T = 0$ (phase-coherent) limit . Since all DC experiments are in the former limit, while the vast majority of theoretical predictions are in the latter, finite frequency measurements can in fact given unique insight. It was predicted by Damle and Sachdev that at the 2D superfluid-insulator transition the conductivity is equal to two different universal numbers of order e^2/h in the $\omega/T \to 0$ and $\omega/T \to \infty$ limits as shown in Fig. 46. This is true even if both ω and T are both asymptotically small.

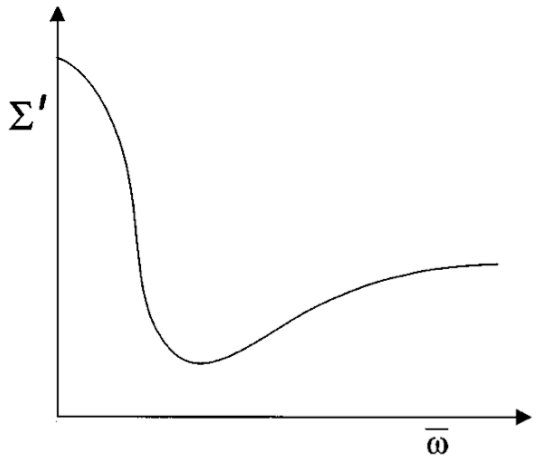

FIG. 46 The real part of universal scaling function Σ, as a function of $\bar{\omega} = \omega/T$. There is a Drude-like peak from the inelastic scattering between thermally exciting carrier, which falls off at order $\bar{\omega} \sim 1$. At larger $\bar{\omega}$ there is a crossover to a collisionless regime. Importantly the function gives different values in the $\bar{\omega} \to 0$ and $\bar{\omega} \to \infty$ limits.

VI. ACKNOWLEDGMENTS

I would like to thank the organizers of the 2008 Boulder School for Condensed Matter Physics for the opportunity to talk about these topics. I'd also like to thank Luke Bilbro, Vladimir Cvetkovic, Natalia Drichko, and Wei Liu for helpful suggestions and careful reading of these lecture notes.

References

[1] Thomas P. Devereaux and Rudi Hackl, Rev. Mod. Phys. 79, 175 (2007).
[2] L.D. Landau, Sov. Phys. JETP 3, 920 (1956); 5, 101 (1957).
[3] D.C. Tsui, H.L. Stormer and A.C. Gossard, Phys. Rev. Lett., 48 1559 (1982).
[4] R.B. Laughlin, Phys. Rev. Lett., 50 1395 (1983).
[5] E. Lieb and F.Y. Wu, Phys. Rev. Lett. 20, 1455 (1968).
[6] A. Schwartz *et al.*, Phys. Rev. B 58, 1455 (1998).
[7] L. Degiorgi *et al.*, Z. Phys. B 102, 367M (1997).
[8] M. Dressel and G. Grüner, "Electrodynamics of Solids: Optical Properties of Electrons in Matter" (Cambridge University Press, 2002).
[9] Stefan J. Turneaure, Aaron A. Pesetski, and Thomas R. Lemberger, J. Appl. Phys. 83, 4334 (1998).
[10] G. D. Mahan, "Many-Particle Physics", (Plenum, 2nd ed., 1990).
[11] O. Klein, S. Donovan, M. Dressel, G. Grüner, *Int. J. Infrared Millim. Waves* **14**, 2423 (1993).
[12] Marc Scheffler, Martin Dressel, Martin Jourdan and Hermann Adrian, "Extremely slow Drude relaxation of correlated electrons", Nature **438**, 1135 (2005).
[13] Marc Scheffler and Martin Dressel, "Broadband microwave spectroscopy in Corbino geometry for temperatures down to 1.7 K", Rev. Sci. Instrum. **76**, 074702 (2005).
[14] James C. Booth, Dong Ho Wu, S. B. Qadri, E. F. Skelton, M. S. Osofsky, Alberto Piqué, and Steven M. Anlage, "Large Dynamical Fluctuations in the Microwave Conductivity of $YBa_2Cu_3O_7 - \delta$ above T_c", Phys. Rev. Lett. **77**, 4438 (1996).
[15] J. C. Booth, Dong Ho Wu, and Steven M. Anlage, "A broadband method for the measurement of the surface impedance of thin films at microwave frequencies", Rev. Sci. Instrum. **65**, 2082 (1994).
[16] M. L. Stutzman, Mark Lee, R. F. Bradley, "Broadband calibration of long lossy microwave transmission lines at cryogenic temperatures using nichrome films", Rev. Sci. Instrum. **71**, 4596 (2000).
[17] M. Lee and M. L. Stutzmann, "Microwave ac Conductivity Spectrum of a Coulomb Glass", Phys. Rev. Lett. **87**, 056402 (2001).
[18] P. J. Turner, D. M. Broun, Saeid Kamal, M. E. Hayden, J. S. Bobowski, R. Harris, D. C. Morgan, J. S. Preston, D. A. Bonn, and W. N. Hardy, "Bolometric technique for high-resolution broadband microwave spectroscopy of ultra-low-loss samples", Rev. Sci. Instrum., Vol. 75, No. 1, January (2004).
[19] `http://www.er.doe.gov/bes/reports/abstracts.html#THz`
[20] R. A. Kaindl, M. A. Carnahan, D. Hägele, R. Lövenich and D. S. Chemla, "Ultrafast terahertz probes of transient conducting and insulating phases in an electron-hole gas", Nature **423**, 734 (2003).
[21] James N. Heyman, Roland Kersting and Karl Unterrainer, "Time-domain measurement of intersubband os-

cillations in a quantum well", Appl. Phys. Lett. 72, 644 (1998).
[22] A. J. Gatesman, J. Waldman, M. Ji, C. Musante, and S. Yngvesson, "An anti-reflection coating for silicon optics at terahertz frequencies", IEEE Microwave Guid. Wave Lett. **10**, 264-266 (2000).
[23] J. S. Dodge, C. P. Weber, J. Corson, J. Orenstein, Z. Schlesinger, J. W. Reiner, M. R. Beasley, "Low-Frequency Crossover of the Fractional Power-Law Conductivity in SrRuO3", Phys. Rev. Lett. **85**, 4932 - 4935 (2000).
[24] J. Corson, R. Mallozzi, J. Orenstein, J. N. Eckstein and I. Bozovic, "Vanishing of phase coherence in underdoped $Bi_2Sr_2CaCu_2O_{8+\delta}$", Nature **398**, 221 (1999).
[25] S. Wang, B. Ferguson, D. Abbott and X.-C. Zhang, "T-ray imaging and tomography," J. Bio. Phys. **29**, 247-256 (2004).
[26] Michael Nagel, Peter Haring Bolivar, Martin Brucherseifer, Heinrich Kurz, Anja Bosserhoff, and Reinhard Büttner, "Integrated Planar Terahertz Resonators for Femtomolar Sensitivity Label-Free Detection of DNA Hybridization", Appl. Opt. **41**, 2074-8 (2002).
[27] B.B. Hu and M.C. Nuss, "Imaging with terahertz waves", Opt. Lett. **20**, 1716 (1995).
[28] X.-C. Zhang, "Terahertz wave imaging: horizons and hurdles", Physics in Medicine and Biology **47**, 1 (2002).
[29] J. L. Johnson, T. D. Dorney, and D. M. Mittleman, "Enhanced depth resolution in terahertz imaging using phase-shift interferometry", Applied Physics Letters, **78**, 835 (2001).
[30] `http://en.wikipedia.org/wiki/Terahertz_time_domain_spectroscopy`.
[31] D. van Mechelen *et al.*, to be submitted App. Phys. Lett.
[32] G.V. Kozlov and V.V. Volkov, in Millimeter and Submillimeter Wave Spectroscopy of Solids, edited by G.Grner (Springer, Berlin, 1998).
[33] W. J. Padilla, Z. Q. Li, K. S. Burch, Y. S. Lee, K. J. Mikolaitis, and D. N. Basov. Review of Scientific Instruments 75, 4710 (2004).
[34] D.N. Basov and T. Timusk, Electrodynamics of high-Tc superconductors, Reviews of Modern Physics 77, 721 (2005).
[35] D.E. Aspnes, Surf. Sci. 37 418 (1973).
[36] D.E. Aspnes and A.A. Studna. Phys. Rev. B 27 985 (1983).
[37] A. Röseler. Infrared Spectroscopic Ellipsometry, Akademie-Verlag, Berlin (1990).
[38] K.L. Barth *et al.*, Thin Solid Films **234** 314 (1993).
[39] J. Bremer, O. Hunderi, K. Faping, T. Skauli and E. Wold, Appl. Optics **31**, 471(1992).
[40] C. Bernhard, J. Humlcek and B. Keimer, Thin Solid Films **455-456**, 143-149, (2004).
[41] A.B. Kuzmenko, "Kramers-Kronig constrained variational analysis of optical spectra", Rev. Sci. Instrum.76, 083108 (2005).
[42] M. Bass and E.W. Van Stryland, (eds.) Handbook of Optics vol. 2 (2nd ed.), McGraw-Hill (1994).
[43] P. B. Johnson and R. W. Christy, "Optical Constants of the Noble Metals", Phys. Rev. B 6, 4370 - 4379 (1972).
[44] H. Ehrenreich, H. R. Philipp, and B. Segall, "Optical Properties of Aluminum", Phys. Rev. 132, 1918 - 1928 (1963).
[45] H. Ehrenreich and H.R. Philipp, Phys. Rev. 128, 1622 (1962).
[46] D. M. Roessler and W. C. Walker, "Electronic Spectra of Crystalline NaCl and KCl", Phys. Rev. 166, 599 - 606 (1968).
[47] G. A. Thomas, M. Capizzi, F. DeRosa, R. N. Bhatt, and T. M. Rice, "Optical study of interacting donors in semiconductors", Phys. Rev. B 23, 5472 - 5494 (1981).
[48] E. Helgren, N.P. Armitage, G. Grüner, Phys. Rev. Lett. 89, 246601 (2002).
[49] E. Helgren, N. P. Armitage, and G. Grüner, Phys. Rev. B 69, 014201 (2004).
[50] N.F. Mott, J. Non-Cryst. Solids 1, 1 (1968).
[51] A.L. Efros and B.I. Shklovskii, J. Phys. C 8, L49 (1975).
[52] M. Lee and M.L. Stutzmann, Phys. Rev. Lett. 30, 056402 (2001).
[53] R.N. Bhatt *private communication*.
[54] P.W. Anderson, Comments Solid State Phys. 2, 193 (1970).
[55] M.B.J. Meinders *et al.*, Phys. Rev. B 48, 3916 (1993).
[56] S. Uchida *et al.*, Phys. Rev. B 43, 7942 (1991).
[57] M. Tinkham, Introduction to Superconductivity, 2nd Ed. , McGraw-Hill, NY, (1996).
[58] L. C. Hebel and C. P. Slichter, Phys. Rev. 107, 901 - 902 (1957).
[59] Leigh Hunt Palmer and M. Tinkham, Phys. Rev. 165, 588 - 595 (1968).
[60] O. Klein, E. J. Nicol, K. Holczer and G. Grner, Phys. Rev. B 50, 6307 - 6316 (1994).
[61] A. Hosseini *et al.* , Phys. Rev. Lett. 93, 107003 (2004).
[62] D. A. Bonn, P. Dosanjh, R. Liang, and W. N. Hardy, Phys. Rev. Lett. 68, 2390 - 2393 (1992).
[63] D. Y. Smith, E. Shiles, Phys. Rev. B 17, 4689 (1978).
[64] H.J.A. Molegraaf, C. Presura, D. van der Marel, P. H. Kes, and M. Li, Science 295, 2239 (2002).
[65] A.V. Boris, N. N. Kovaleva, O. V. Dolgov, T. Holden, C. T. Lin, B. Keimer, and C. Bernhard, Science 304, (2004).
[66] J. W. Allen and J. C. Mikkelsen, "Optical properties of CrSb, MnSb, NiSb, and NiAs", Phys. Rev. B 15, 2952 - 2960 (1977).
[67] S.J. Youn, phys. stat. sol. (b) , No. 4, 13541362 (2007).
[68] A. Millis and P.A. Lee, "Large-orbital-expansion for the lattice Anderson model", Phys. Rev. B 35, 3394 (1987).
[69] P.B. Allen, Phys Rev. B 3, 305 (1971).
[70] R. R. Joyce and P. L. Richards, Phys. Rev. Lett. 24, 1007 - 1011 (1970).
[71] A. M. Awasthi, L. Degiorgi, G. Grüner, Y. Dalichaouch, and M. B. Maple, Phys. Rev. B 48, 10692, (1993).
[72] A. V. Puchkov, D. N. Basov, and T. Timusk, J. Phys.: Condens. Matter 8 (1996) 10049-10082.
[73] F. Marsiglio, J. P. Carbotte, and E. Schachinger, Phys. Rev. B 65, 014515 (2001).
[74] J. Carbotte, E. Schachinger, and D. N. Basov, Nature (London) 401, 354 (1999).
[75] R. Tediosi *et al.*, Phys. Rev. Lett. 99, 016406 (2007).
[76] B. Lundqvist, Phys. Kondens. Mater. 6, 193 (1967).
[77] B. Lundqvist, Phys. Status Solidi 32, 273 (1969).
[78] J. Hwang, T. Timusk, and G. D. Gu, Nature 427, 714 (2004)
[79] S. L. Sondhi *et al.*, Rev. Mod. Phys. **69**, 315 (1997).
[80] S. Sachdev, *Quantum Phase Transitions*, Cambridge University Press (1999).
[81] H. E. Stanley, Introduction to Phase Transitions and Critical Phenomena Oxford University Press, Oxford, 1971.
[82] D. van der Marel *et al.*, Nature 425, 271-274 (18 Septem-

ber 2003).
[83] L.W. Engel, D. Shahar, C. Kurdak, and D.C. Tsui, 1993, Phys. Rev. Lett. 71, 2638.
[84] H.P. Wei, D.C. Tsui, M.A. Paalanen, and A.M.M. Pruisken, Phys. Rev. Lett. 61, 1294. (1988).
[85] H.-L. Lee, J. P. Carini, D. V. Baxter, G. Grüner, Phys. Rev. Lett. 80, 4261-4264 (1998).
[86] H.-L. Lee, J.P. Carini, D.V. Baxter, W. Henderson, and G. Grüner, "Quantum-Critical Conductivity Scaling for a Metal-Insulator Transition", Science 287, 633-6 (2000).
[87] D. Belitz and T. R. Kirkpatrick, Rev. Mod. Phys. 66, 261 (1994).
[88] Kedar Damle and Subir Sachdev, "Nonzero-temperature transport near quantum critical points", Phys. Rev. B 56, 8714 (1997).